Hydrol. Earth Syst. Sci. Discuss., 11, 11637–11686, 2014
www.hydrol-earth-syst-sci-discuss.net/11/11637/2014/
doi:10.5194/hessd-11-11637-2014
© Author(s) 2014. CC Attribution 3.0 License.

Hydrology and Earth System Sciences
Open Access
Discussions

This discussion paper is/has been under review for the journal Hydrology and Earth System Sciences (HESS). Please refer to the corresponding final paper in HESS if available.

Extreme value statistics of scalable data exemplified by neutron porosities in deep boreholes

A. Guadagnini[1,2], S. P. Neuman[1], T. Nan[1], M. Riva[1,2], and C. L. Winter[1]

[1]Department of Hydrology and Water Resources, University of Arizona, Tucson, Arizona, 85721, USA
[2]Dipartimento di Ingegneria Civile e Ambientale, Politecnico di Milano, Piazza L. Da Vinci 32, 20133 Milano, Italy

Received: 24 September 2014 – Accepted: 1 October 2014 – Published: 22 October 2014

Correspondence to: T. Nan (tcnan.nju@gmail.com)

Published by Copernicus Publications on behalf of the European Geosciences Union.

Abstract

Spatial statistics of earth and environmental (as well as many other) data tend to vary with scale. Common manifestations of scale-dependent statistics include a tendency of increments to have symmetric, non-Gaussian frequency distributions characterized by heavy tails that decay with separation distance or lag; power-law scaling of sample structure functions (statistical moments of absolute increments) in midranges of lags; linear relationships between log structure functions of successive orders at all lags, known as extended self-similarity or ESS; and nonlinear scaling of structure function power-law exponents with function order, a phenomenon commonly attributed in the literature to multifractals. Elsewhere we proposed, explored and demonstrated a new method of geostatistical inference that captures all of these phenomena within a unified theoretical framework. The framework views data as samples from random fields constituting scale-mixtures of truncated (monofractal) fractional Brownian motion (tfBm) or fractional Gaussian noise (tfGn). Important questions not addressed in previous studies concern the distribution and statistical scaling of extreme incremental values. Of special interest in hydrology (and many other areas) are statistics of absolute increments exceeding given thresholds, known as peaks over thresholds or POTs. In this paper we explore for the first time the statistical behavior of POTs associated with samples from scale-mixtures of tfBm or tfGn. We are fortunate to have at our disposal thousands of neutron porosity values from six deep boreholes, in three diverse depositional environments, which we show possess the properties of such samples thus following the theory we proposed. The porosity data are of additional value in revealing a remarkable transition from one scaling regime to another at certain lags. The phenomena we uncover are of fundamental importance for the analysis of fluid flow and solute as well as particulate transport in complex hydrogeologic environments.

HESSD
11, 11637–11686, 2014

1 Introduction

The statistics of extremes has received much attention among hydrologists (Katz et al., 2002) and others concerned with a wide range of phenomena including snow avalanches on mountain slopes (Ancey, 2012); rupture events associated with the propagation of cracks or sliding along faults in brittle materials including rock failure, landslides and earthquakes (Amitrano, 2012; Lei, 2012; Main and Naylor, 2012) as well as volcanic eruptions, landslides, wildfires and floods (Sachs et al., 2012; Schoenberg and Patel, 2012; Süveges and Davison, 2012); demographic and financial crises (Akaev et al., 2012; Janczura and Weron, 2012); neuronal avalanches and coherence potentials in the mammalian cerebral cortex (de Arcangelis, 2012; Plenz, 2012); citations of scientific papers (Golosovsky and Solomon, 2012); and distributions of city sizes (Pisarenko and Sornette, 2012). Extreme values cluster around heavy tails of data frequency distributions which are often modeled as stretched exponential, lognormal or power functions. There is growing evidence that these frequency distributions, as well as other geospatial and/or temporal statistics of many data, vary with scale. A key related question concerns the scale dependence of frequency distributions (typically generalized extreme value or GEV in the case of block extrema and generalized Pareto distribution or GPD in the case of peaks over thresholds or POTs, e.g., Embrechts et al., 1997) and statistics of extremes at the tails of the original data distributions (e.g., Riva et al., 2013a). Here we address this question vis-à-vis POTs of neutron porosity values from six deep boreholes in three different depositional environments. These data are of interest because, as we show below, (a) they possess statistics that scale in manners typical of many earth, environmental and other variables and (b) reveal a remarkable transition from one scaling regime to another at certain separation distances or lags. The phenomena we uncover vis-a-vis neutron porosity data, and corresponding extremes, are of fundamental importance for the analysis of fluid flow and solute as well as particulate transport in complex hydrogeologic environments. They are particularly relevant to depositional processes responsible for the development of preferential flow

HESSD
11, 11637–11686, 2014

paths through heterogenous porous and fractured media. Neutron porosity logs are widely used to characterize stratigraphic sequences and the geostatistical structures of lithotypes in multilayer systems of aquifers and aquitards (e.g., Barrash and Reboulet, 2004; Tronicke and Holliger, 2005). Combined with laboratory-determined particle size distributions, porosity data may allow one to infer spatial distributions (see review of Vuković and Soro, 1992) and covariances (Riva et al., 2014) of hydraulic conductivity.

Whereas research in the subsurface hydrology literature has not specifically addressed the distribution and statistical scaling of extreme incremental values, spatial correlations between values significantly in excess of the mean have been studied vis-à-vis variables such as transmissivity and their relevance to transport processes has been highlighted. Sanchez-Vila et al. (1996) conjectured that observed scale dependence of transmissivities estimated from large scale pumping tests could be related to strong connectivity between regions of elevated transmissivity, as opposed to spatial persistence of average or low transmissivity values. Spatial correlation of extreme conductivity values was examined for the first time by Gómez-Hernández and Wen (1998). In these authors' opinion the standard multi-Gaussian assumption was not consistent with observed short solute travel times resulting from fast spatially connected pathways. Connectivity of high permeability zones thus became an important concept underlying some modern interpretations of effective conductivity and solute travel time (see for example Meier et al., 1998; Wen and Gómez-Hernández, 1998; Western et al., 2001; Fogg et al., 2000; Zinn and Harvey, 2003; Knudby and Carrera, 2005, 2006; Knudby et al., 2006; Nield, 2008, and references therein). The above ideas have motivated the development of multi-point geostatistical methods of analysis such as those described in a recent special issue of the journal *Mathematical Geosciences* on 20 years of multi-point statistics (e.g., Renard and Mariethoz, 2014; Mariethoz and Renard, 2014, and references therein).

Otherwise, attempts by hydrologists to investigate the manner in which statistics of extremes vary with scale have centered almost exclusively on peak rainfall intensities and stream flows. Whereas some have found statistical measures of rainfall extremes

HESSD
11, 11637–11686, 2014

to exhibit linear (sometimes termed simple) scaling (Menabde et al., 1999; Garcia-Bartual and Schneider, 2001; De Michele et al., 2001) under at least some conditions (Burlando and Rosso, 1996; Veneziano and Furcolo, 2002; Yu et al., 2004), most authors describe them by means of nonlinear (often called multiscaling) models (Burlando and Rosso, 1996; Veneziano and Furcolo, 2002; Castro et al., 2004; Langousis and Veneziano, 2007; Mohymont and Demarée, 2006). Statistical measures of peak stream flows were considered by Javelle et al. (1999), Menabde and Sivapalan (2001) and Rigon et al. (2011) to scale linearly. Work on the scaling of GEVs and/or GPDs associated with extreme rainfall and/or stream flow was reported amongst others by Nguyen et al. (1998), Menabde et al. (1999), Menabde and Sivapalan (2001), Willems (2000), Trefry et al. (2005), Veneziano et al. (2009) and Veneziano and Yoon (2013). The general tendency has been to interpret linear scaling as a manifestation of monofractal behavior analogous to that of fractional Brownian motion (fBm) or fractional Gaussian noise (fGn). Nonlinear scaling has commonly been attributed to multifractal behavior, a viewpoint espoused originally by Schertzer and Lovejoy (1987) and expanded on recently by Veneziano and Yoon (2013).

Work by our group has demonstrated theoretically (Neuman, 2010, 2011; Guadagnini and Neuman, 2011; Siena et al., 2012; Neuman et al., 2013), computationally (Guadagnini et al., 2012; Neuman et al., 2013) and on the basis of varied pedological, hydrological and hydrogeological data (Siena et al., 2012, 2014; Riva et al., 2013b, c; Guadagnini et al., 2012, 2013, 2014) that statistical scaling behaviors of the kind traditionally attributed to multifractals can be interpreted more simply and consistently by viewing the data as samples from stationary sub-Gaussian random fields subordinated to truncated fBm (tfBm) or fGn (tfGn). Such sub-Gaussian fields are scale mixtures of stationary Gaussian fields with random variances (Andrews and Mallows, 1974; West, 1987) that we model as being log-normal or Lévy stable (Samorodnitsky and Taqqu, 1994). In this sense our approach bears partial relationship to cascades of Gaussian-scale mixtures that Ebtehaj and Foufoula-Georgiou (2011) use to reproduce coherent structures and extremes of precipitation reflectivity images in the wavelet domain.

HESSD
11, 11637–11686, 2014

In this paper we employ our novel method of data interpretation to investigate the scaling of statistics characterizing vertical increments in borehole neutron porosity data and associated POTs and demonstrate that these data display statistical scaling consistent with our theoretical framework. Our analysis suggests that, quantitatively, the statistics of neutron porosity increments and their POTs at intra-layer vertical separation scales (or lags) differ from those at inter-layer scales. Qualitatively, however, the statistics of porosity increments at each of these two scales behave in a manner that the literature would typically associate with multifractals. This behavior includes tendency of increments to have symmetric, non-Gaussian frequency distributions characterized by heavy tails that often decay with separation distance or lag; power-law scaling of sample structure functions (statistical moments of absolute increments) in midranges of lags, with breakdown in power-law scaling at small and/or large lags; linear relationships between log structure functions of successive orders at all lags, also known as extended self-similarity or ESS; and nonlinear scaling of structure function power-law exponents with function order. Our alternative interpretation of the data allows us to obtain maximum likelihood estimates of all parameters characterizing the underlying truncated sub-Gaussian fields at both intra- and inter-layer scales. Most importantly, we offer what appears to be the first data-driven exploration (following a synthetic study of outliers by Riva et al., 2013a) of how statistics of POTs associated with such families of sub-Gaussian fields vary with scale.

2 Source and frequency distributions of neutron porosity data

As stated in Sect. 1, we illustrate and explore our approach on neutron porosity data from six deep vertical boreholes in three different depositional environments. These are part of a broader set of geophysical logs from the same boreholes, previously described and analyzed within a multifractal framework by Dashtian et al. (2011), provided to us courtesy of Muhammad Sahimi, University of Southern California. Three of the wells (numbered here 1, 2 and 3) are drilled in the Maroon field within which gas drive is

HESSD
11, 11637–11686, 2014

used to produce oil and natural gas, wells 4 and 5 in the Ahwaz oil field, and well 6 in the Tabnak gas field. The Maroon and Ahwaz fields in southwestern Iran, and the Tabnak field in southern Iran, have distinct geologies. Whereas carbonate rock content is highest in the Tabnak and lowest in the Maroon and Ahwaz fields, the opposite is true about sandstone content. Though we do not have information about the relative geographic locations of the six wells, we note that Dashtian et al. (2011) analyzed data from each well independently of those from the remaining five wells. We do the same on the assumption that distances between the wells are sufficiently large to allow treating data from each well as being statistically independent of the rest.

Summary information about the available neutron porosity (P) data is listed in Table 1. As the sampling interval between available values in Well 6 is half of that in Wells 1–5, we disregard every other measurement in analyzing these data, leaving a total of 4267 values. Figure 1 shows how the neutron porosity data vary with depth in Wells 1, 4, 5 and 6. Frequency distributions of deviations, $P' = P - P_a$, from average values, P_a, in Wells 1, 4 and 6 are plotted on arithmetic and semi-logarithmic scales in Fig. 2. The empirical frequency distributions exhibit sharp peaks, asymmetry and slight bimodality. Also shown in Fig. 2 are maximum likelihood (ML) fits of a Gaussian and two sub-Gaussian probability density functions (pdfs) to the empirical frequency distributions. Sub-Gaussian random variables, defined in Appendix A, are scale mixtures of Gaussian variables with random variances. We consider two sub-Gaussian variables, one α-stable with Gaussian variances that are α-stable, and another normal-lognormal (NLN) variable with lognormal Gaussian variances. ML fits to Gaussian and α-stable pdfs is accomplished with a code developed by Nolan (2001) and to NLN using a code we have written in Matlab. The quality of these fits is variable; in the case of Well 1, the NLN model is seen to fit the empirical frequency distribution slightly better than do the other two models but, in the case of Well 6, the α-stable model is seen to be best and Gaussian model worst. Formal Kolmogorov–Smirnov, χ^2 and Shapiro–Wilk tests conducted on some of the data tend to reject the Gaussian model at a significance level of 0.05.

HESSD
11, 11637–11686, 2014

3 Frequency distributions of neutron porosity increments

The remainder of our analysis concerns increments in recorded P values along various separation distances s, or lags, in each well. Lags are taken to be integer multiples, $s = s_n \times \Delta z$, of the vertical spacing, $\Delta z = 0.1524$ m, between recorded values. Rather than presenting results in terms of s we report them below in terms of normalized (by Δz) integer values, s_n. Figure 3 shows how increments $\Delta P(s_n)$ at three different normalized lags ($s_n = 1$, 32, 1024) vary with sequential (integer) vertical position in Wells 1 (Maroon field), 4 (Ahwaz field) and 6 (Tabnak field).

Frequency distributions of $\Delta P(s_n)$ at the same three lags in Wells 1 and 4 are plotted on semi-logarithmic scale in Fig. 4. The empirical frequency distributions exhibit pronounced symmetry with sharp peaks and heavy tails, which decay toward Gaussian shapes as lags increase. At all lags, the empirical frequency distributions of increments are represented quite closely by α-stable and NLN models fitted to them by ML. Negative log likelihood (NLL) measures of best fit associated with these two models as well as values of the Kashyap (1982) information criterion, KIC, demonstrate that they fit the empirical frequency distributions equally well (not shown). The same is true for all increments in all other wells. Frequency distributions of $\Delta P(s_n)$ plotted for two normalized lags in Well 6 (Fig. 5) are likewise symmetric with sharp peaks and heavy tails which, however, do not decay with lag. Empirical frequency distributions of $\Delta P(s_n)$ in Well 6 are represented equally well by α-stable and NLN models.

Figure 6 shows how estimates $\hat{\alpha}$ and $\hat{\sigma}$ of stability and scale parameters, respectively, characterizing α-stable distribution models (see Appendix A) of neutron porosity increments in all wells vary with normalized lag. Estimates $\hat{\alpha}$ of the stability index, α, in Wells 1–3 (Maroon field) and 4–5 (Ahwaz field) exceed 1 and increase asymptotically toward 2 with increasing lag, confirming that the increments become Gaussian at large lags. In Well 6 (Tabnak field) $\hat{\alpha}$ fluctuates around a value that exceeds 1 by a small amount. Estimates $\hat{\sigma}$ of the scaling index σ, which measures the width of the α-stable distribution, first increase with lag and then stabilize in all wells. All these behaviors

HESSD
11, 11637–11686, 2014

are consistent with sub-Gaussian random fields associated with α-stable subordinators; whether or not α does or does not grow with lag depends on how these fields are generated (see Riva et al., 2013c; Neuman et al., 2013). We do not show but note that parameters of NLN distribution models fitted to the increments also vary with lag in a way that renders them asymptotically Gaussian at large lags, with the exception of Well 6.

4 Statistical scaling of neutron porosity increments

Next we analyze the scaling behavior of sample structure functions, $S_N^q(s_n)$, of order q based on $N(s_n)$ absolute increments at normalized lag s_n,

$$S_N^q(s_n) = \frac{1}{N(s_n)} \sum_{j=1}^{N(s_n)} |\Delta P_j(s_n)|^q. \quad (1)$$

Figure 7 shows how such structure functions of orders $q = 0.5$, 1.0 and 2.0 vary with s_n in Wells 1 (Maroon) and 6 (Tabnak). Log-log regression lines fitted to the data separately at vertical distance scales $s_n < 10$ and $s_n > 12$ suggest, at relatively high levels of confidence (coefficients of determination, R^2, ranging from 0.98 to 0.99 at $s_n < 10$ and from 0.89 to 0.99 at $s_n > 12$), that $S_N^q(s_n)$ varies as a power of s_n in each of these two scale ranges. Power-law exponents are larger at small ($s_n < 10$) than at large ($s_n > 12$) lags. We thus have a break in power-law regime at distance scales 1.5–1.8 m delineated in Fig. 7 by a dashed red line. We interpret the power-law scaling of $S_N^q(s_n)$ with s_n at $s_n < 10$ to represent variability within, and that at $s_n > 12$ variability between, sedimentary layers at each site. Similar dual power-law scaling behavior is exhibited by structure functions of increments from Wells 2–5 (not shown). A similar dual-scaling phenomenon has recently been reported by Siena et al. (2014) vis-a-vis porosities and specific surface areas imaged using x-ray computer micro-tomography throughout a millimeter-scale block of Estaillades limestone, at a spatial resolution of 3.3 µm, as

HESSD
11, 11637–11686, 2014

well as Lagrangian velocities computed by solving the Stokes equation in the sample pore space.

Following the most recent examples of Guadagnini et al. (2013, 2014) we use the method of moments to obtain estimates, $\hat{H}_w$ and $\hat{H}_b$, of Hurst scaling exponents, H_w and H_b, characterizing the within- and between-layers scaling behaviors of neutron porosity increments, respectively, in each well. $\hat{H}_w$ and $\hat{H}_b$ are set equal to the slopes, $\xi_w(q=1)$ and $\xi_b(q=1)$, of regression lines fitted to $S_N^1(s_n)$ on log–log scale at $s_n < 10$ and $s_n > 12$, respectively. Values of these estimates are listed, for all six wells, in Table 2. As $\hat{H}_w > 1/\hat{\alpha}$ and $\hat{H}_b \ll 1/\hat{\alpha}$ in all cases, we conclude that whereas intra-layer variability is persistent (large values tend to follow large values and small values tend to follow small values), inter-layer variability is strongly antipersistent (small and large values tend to alternate rapidly). The latter is likely a manifestation of strong variations in environments responsible for the deposition of alternating sedimentary layers.

As no theory other than ours (Siena et al., 2012; Neuman et al., 2013) is known to explain extended self-similarity (ESS) of variables that do not necessarily satisfy Burger's equation (Chakraborty et al., 2010), demonstrating that $\Delta P(s_n)$ satisfy ESS is akin to verifying that these data conform to our theoretical scaling framework. That this is indeed the case becomes evident upon examining the high-confidence (R^2 = 0.91–0.99) straight line relationships between $\log S_N^{q+1}$ and $\log S_N^q$, and corresponding power-law relationships between S_N^{q+1} and S_N^q, at $s_n < 10$ and $s_n > 12$ in Fig. 8 for q = 1, 2 and 3 in Wells 1 (Maroon) and 6 (Tabnak). Similar ESS relationships hold (not shown) in Wells 2–5.

Our next step is to compute functional relationships between power exponents $\xi_w(q)$ and $\xi_b(q)$, and the order q, of structure functions that scale as power-laws of lag. In the method of moments these powers are the slopes of regression lines fitted to log–log plots of $S_N^q(s_n)$ vs. s_n, such as those depicted in Fig. 7. In the case of ESS we use $\xi_w(q=1)$ and $\xi_b(q=1)$, determined by the method of moments, as reference values for the sequential computation of $\xi_w(q)$ and $\xi_b(q)$ at $q > 1$ based on known power-law relationships between S_N^{q+1} and S_N^q, such as those given in Fig. 8. Corresponding plots

HESSD
11, 11637–11686, 2014

of $\xi_w(q)$ and $\xi_b(q)$ as functions of q, evaluated by the method of moments and ESS in Wells 1 and 6 at $s_n < 10$ and $s_n > 12$, are presented in Fig. 9. Results obtained by the two methods are, for the most part, very similar. With the exception of $\xi_w(q)$ at $s_n < 10$ in Wells 1, 2, and 3 (Maroon field), in all cases (including those corresponding to Wells 2–5, which we do not show) $\xi_w(q)$ and $\xi_b(q)$ delineate convex functions that fall below straight lines having slopes $\hat{H}_w$ and $\hat{H}_b$, respectively, which pass through the origin. Tradition has it that whereas such straight lines are characteristic of monofractal (self-affine, additive) random fields, nonlinear variations of power exponents such as those exhibited by $\xi_w(q)$ and $\xi_b(q)$ in Fig. 9 are symptomatic of (multiplicative) multifractals. Yet we have seen that the data in this paper conform to a statistical scaling theory in which the underlying random fields are subordinated to truncated versions of monofractal fBm or fGn. As we have previously demonstrated theoretically (Neuman, 2010, 2011; Neuman et al., 2013) and computationally (Guadagnini et al., 2012), nonlinear scaling of such data is nothing but a random artifact of sampling from similar fields.

5 Estimation of variogram parameters

We have seen that our analysis supports treating the neutron porosity data from each well as a random sample from a stationary sub-Gaussian random field subordinated to tfBm or tfGn. Let $G'(x;\lambda_l,\lambda_u)$ denote zero-mean tfBm, defined by Di Federico and Neuman (1997) as a Gaussian random function of x having variance

$$\sigma^2_G(\lambda_l,\lambda_u) = \sigma^2_G(\lambda_u) - \sigma^2_G(\lambda_l), \tag{2}$$

variogram or semi-structure function of second order

$$\gamma_G(s;\lambda_l,\lambda_u) = \gamma_G(s;\lambda_u) - \gamma_G(s;\lambda_l), \tag{3}$$

HESSD
11, 11637–11686, 2014

and integral autocorrelation scale

$$I(\lambda_l, \lambda_u) = \frac{2H}{1+2H} \frac{\lambda_u^{1+2H} - \lambda_l^{1+2H}}{\lambda_u^{2H} - \lambda_l^{2H}} \quad (4)$$

where, for $m = l, u$,

$$\sigma_G^2(\lambda_m) = A\lambda_m^{2H}/2H, \quad (5)$$

$$\gamma_G(s;\lambda_m) = \sigma_G^2(\lambda_m)\rho(s/\lambda_m), \quad (6)$$

A is a coefficient, H is a Hurst scaling exponent and s is lag. The tfBm variogram $\gamma_G(s;\lambda_l,\lambda_u)$ is a weighted integral of variograms characterizing stationary Gaussian fields, or modes, having integral scales λ and variances $\sigma^2(\lambda) = A\lambda^{2H}/2H$, between lower and upper cutoff scales, λ_l and λ_u, respectively. Here we consider modes having Gaussian variograms in which case

$$\rho(s/\lambda_m) = \left[1 - \exp\left(-\frac{\pi}{4}\frac{s^2}{\lambda_m^2}\right) + \left(\frac{\pi}{4}\frac{s^2}{\lambda_m^2}\right)^H \Gamma\left(1-H, \frac{\pi}{4}\frac{s^2}{\lambda_m^2}\right)\right] \qquad 0 < H < 1 \quad (7)$$

where $\Gamma(\cdot,\cdot)$ is the incomplete gamma function. In the limits $\lambda_l \to 0$ and $\lambda_u \to \infty$, $\gamma_G(s;\lambda_l,\lambda_u)$ tends to a power variogram (PV) $\gamma^2(s) = Bs^{2H}$ where $B = A(\pi/4)^{2H/2}\Gamma(1-2H/2)/2H$, Γ being the gamma function. The stationary tfBm $G'(x;\lambda_l,\lambda_u)$ thus tends to nonstationary fBm, $G'(x;0,\infty)$, the stationary increments of which, $\Delta G(x, x+s;0,\infty)$, form fGn. It follows that when $\lambda_u < \infty$, $\gamma_G(s;\lambda_l,\lambda_u)$ is a truncated power variogram (TPV) characterizing a (stationary) truncated version of fBm (tfBm).

We treat neutron porosity increments in each borehole as a sample from a zero-mean random field, $\Delta Y(x, x+s;\lambda_l,\lambda_u)$, subordinated to tfBm according to (see Appendices A and B)

$$\Delta Y(x, x+s;\lambda_l,\lambda_u) = W^{1/2}\Delta G(x, x+s;\lambda_l,\lambda_u) \quad (8)$$

HESSD
11, 11637–11686, 2014

where $s \geq 0$ is lag and the subordinator, $W^{1/2}$, is a non-negative random variable independent of ΔG (and of G'). Based on our earlier findings regarding the frequency distributions of incremental neutron porosity data, we allow $W^{1/2}$ to be Lévy stable or log-normal. Appendix A explains that, in the first case, $W^{1/2}$ is $\alpha/2$-stable totally skewed to the right of zero (hence non-negative) with scale parameter $\sigma_S = \left(\cos\frac{\pi\alpha}{4}\right)^{2/\alpha}$, unit skewness and zero shift. The corresponding univariate pdf of $\Delta Y(x, x+s; \lambda_l, \lambda_u)$ is symmetric α-stable with zero skewness and shift. The pdf possesses heavy, power-law tails. In the second case $W^{1/2} = e^V$ where V is zero-mean Gaussian with variance $\sigma_V^2 = (2-\alpha)^2$. This renders $W^{1/2} \equiv 1$ when $\alpha = 2$ and its pdf increasingly skewed to the right as α diminishes. The corresponding univariate normal–lognormal (NLN) pdf of $\Delta Y(x, x+s; \lambda_l, \lambda_u)$ possesses heavier tails than the exponential tails of the Gaussian to which NLN tends asymptotically as α increases toward 2. Whereas α-stable variables do not possess finite moments of order $\geq \alpha$, all moments of NLN variables are finite.

Our previous ML fits of univariate α-stable and NLN pdf models to neutron porosity increments in each well have yielded estimates of all parameters characterizing these models. We also found the data to exhibit different modes of scaling at $s_n < 10$ and $s_n > 12$ and obtained estimates of H for each of these two ranges of lags. All that remains to fully characterize the multivariate random fields, $\Delta Y(x, x+s; \lambda_l, \lambda_u)$, which we take to underlie the incremental data is to estimate the parameters A, λ_l and λ_u (and, optionally, H) of TPVs corresponding to $s_n < 10$ and $s_n > 12$. We do so next for each of the above two subordinators.

Assuming first that neutron porosity increments in each well are α-stable, one can estimate the scale parameter $\sigma(s; \lambda_l, \lambda_u)$ of their distribution at any lag, s, from the theoretical relationship (Samorodnitsky and Taqqu, 1994)

$$\hat{\sigma}(s; \lambda_l, \lambda_u) = \sqrt{\gamma_G(s; \lambda_l, \lambda_u)}. \quad (9)$$

Here we employ this relationship separately for normalized lag ranges $s_n < 10$ and $s_n > 12$. We saw earlier that structure functions of neutron porosity data in both lag

HESSD
11, 11637–11686, 2014

ranges, including second-order structure functions can be closely represented in each well by power laws. In other words, the TPVs within these lag ranges are effectively PVs. We recall that this happens in the limits as λ_l and λ_u tend, respectively, to zero and infinity. Accordingly, we set $\lambda_l = 0$ and λ_u to a sufficiently large number to insure that the TPV $\gamma_G(s;\lambda_l,\lambda_u)$ reduces, within both working lag ranges, to the PV $\gamma^2(s) = Bs^{2H}$. Then, in a manner analogous to that outlined most recently by Guadagnini et al. (2013, 2014), we obtain ML estimates $\hat{A}$ of A in two ways, once by adopting corresponding method-of-moment estimates $\hat{H}_w$ and $\hat{H}_b$ from Table 2 and once by estimating the latter jointly with A. Both sets of estimates are obtained upon fitting the theoretical PV $\gamma^2(s) = Bs^{2H}$ to sample scale parameters $\hat{\sigma}(s_n)$ such as those plotted vs. s_n in Fig. 7b. The fits are depicted graphically in Fig. 10 for Wells 1 and 6. The corresponding parameter estimates and 95 % confidence limits are listed, for all wells and both lag ranges, in Table 3. The two sets of estimates lie within each other's 95 % confidence intervals, implying that they are equally reliable.

Next we consider the case where neutron porosity increments in each well are NLN. Due to finiteness of all (statistical) moments associated with this model, structure functions of order $q = 2$ in Fig. 7 coincide with twice the variogram of neutron porosity. As shown in Appendix B, the variogram of $Y'(x;\lambda_l,\lambda_u)$ is given by

$$\gamma_Y(s_n;\lambda_l,\lambda_u) = \left(\mu_W^2 + \sigma_W^2\right)\gamma_G(s_n;\lambda_l,\lambda_u) \tag{10}$$

where μ_W and σ_W^2 are defined in Eq. (A1), Appendix A. We replace Eq. (10) by $\gamma_Y(s) = Cs^{2H}$ and fit the latter by ML to second-order sample structure functions of porosity increments in each well, separately for $s_n < 10$ and $s_n > 12$. Joint estimates of C and H for each range of lags, as well as ML estimates of C based on method-of-moment estimates $\hat{H}_w$ and $\hat{H}_b$ from Table 2, together with associated 95 % confidence intervals, are listed in Table 4. Corresponding best fits are depicted graphically in Fig. 11. Here again the two sets of estimates lie within each other's 95 % confidence intervals, implying that they are equally reliable.

HESSD
11, 11637–11686, 2014

6 Frequency distributions of peaks over thresholds

Extreme value analyses of randomly varying data typically concern block maxima (BM) and/or peaks over thresholds (POTs). The number of neutron porosity increments, $\Delta P(s_n)$, available to us at any normalized lag at any well are insufficient to conduct a statistically meaningful analysis of BM. For this reason, and for the fact that POTs provide a higher resolution of maxima than do BM, we focus in this paper exclusively on the former. In way of illustration we consider absolute increments $|\Delta P(s_n)|$ to constitute POTs whenever they exceed a non-negative threshold, u_t, equal to the 95 % quantile of $|\Delta P(s_n)|$ values in a sample. This renders about 5 % of all sampled $|\Delta P(s_n)|$ values POTs. Figure 12 identifies POTs associated with sequences of porosity increments depicted in Fig. 3.

Figure 13 depicts sample autocorrelations of non-overlapping neutron porosity increments at normalized lags s_n = 1, 32 and 96 in Well 1 as functions of similarly normalized vertical distance between the centers of corresponding increments, normalized further by s_n. Autocorrelation is seen to diminish rapidly with the number, n, of these normalized increments in line with theoretical expressions Eqs. (18)–(20) of Neuman (2010), the same being true for all other wells. We expect autocorrelations between POTs to be weaker, possibly justifying a representation of their frequency distributions by generalized Pareto distributions (GPDs) which, theoretically, apply to independent identically distributed (iid) variables. To test this, we plot in Fig. 14 quantile–quantile (Q–Q) plots of GPD fits to frequency distributions of POTs identified in Fig. 12. Included in Fig. 14 are 95 % confidence intervals of these fits and p values of Kolmogorov–Smirnov (KS) goodness of fit tests. A list of POT sample sizes and p values associated with the same three lags in all wells is provided in Table 5. As all p values exceed 0.05, one cannot reject (at a significance level of 95 %) the null hypothesis that all POTs have GPDs.

Figure 15 shows variations of best fit GPD shape (ξ_{POT}) and scale (σ_{POT}) parameters with normalized lag, and corresponding 95 % uncertainty bounds, in the same wells as

HESSD
11, 11637–11686, 2014

in Fig. 14. With the exception of Well 6 in which ξ_{POT} first diminishes with lag and then stabilizes, this parameter fluctuates but does not vary systematically with lag. The same applies to the shape parameter of each fitted GPD. On the other hand σ_{POT} in all wells increases as a power of lag before stabilizing at larger lags, as does the scale parameter of α-stable distributions fitted to all neutron porosity increments in Fig. 6b.

7 Statistical scaling of peaks over thresholds

We end our analysis by exploring the scaling behavior of q-order sample structure functions of POT in absolute increments $|\Delta P_{POT,j}(s_n)|$,

$$S^q_{N_{POT}}(s_n) = \frac{1}{N_{POT}(s_n)} \sum_{j=1}^{N_{POT}(s_n)} |\Delta P_{POT,j}(s_n)|^q \quad (11)$$

where $N_{POT}(s_n)$ is the number of POTs at normalized lag s_n. We do so as we did earlier for all increments. Figure 16 depicts variations of $S^q_{N_{POT}}(s_n)$ with normalized lag for $q = 0.5$, 1.0, and 2.0 in Wells 1 (Maroon) and 6 (Tabnak). A red dashed line in the figure demarcates breaks in power-law scaling regimes at $s_n < 10$ and $s_n > 12$. Included in Fig. 16 are logarithmic scale regression lines and corresponding power-law relations between $S^q_{N_{POT}}(s_n)$ and s_n in each well and scaling regime. The scaling behavior in Fig. 16 is similar to that shown previously for all (unfiltered) porosity increments in Fig. 7. Corresponding estimates of Hurst exponent are listed in Table 6; these too differ little from those obtained earlier for all porosity increments (Table 2) with the exception of estimates $\hat{H}_b$ which are consistently lower than those associated with unfiltered increments. Like the latter (Fig. 8), POTs exhibit ESS at all lags in the scaling intervals $s_n < 10$ and $s_n > 12$ (not shown).

Our final step is to compute functional relationships between power exponents $\xi_w(q)$ and $\xi_b(q)$, and the order q, of POT structure functions that scale as power-laws of lag. We do so as we did previously for unfiltered porosity increments. Corresponding plots

HESSD
11, 11637–11686, 2014

of $\xi_w(q)$ and $\xi_b(q)$ as functions of q, evaluated by the method of moments and ESS in Wells 1 and 6 at $s_n < 10$ and $s_n > 12$, are presented in Fig. 17. Results obtained by the two methods are again, for the most part, very similar. Similar behavior has been shown by us elsewhere (Guadagnini et al., 2012) to be consistent with increments sampled from random fields subordinated to tfBm or tfGn.

8 Conclusions

After showing that neutron porosity data from six deep boreholes in three geologic environments have statistical scaling properties characteristic of samples from scale-mixtures of truncated fractional Brownian motion (tfBm) or fractional Gaussian noise (tfGn), we used these data to explore the statistical behavior of extreme porosity increments the absolute values of which exceed certain thresholds. We expect our results to hold for many earth, environmental and other variables that were shown elsewhere to possess similar statistical scaling properties. These results include the following:

1. The frequency distributions of neutron porosities in any well, or group of wells in any one of the three geologic environments, are non-Gaussian with sharp peaks, asymmetry and slight bimodality.

2. The frequency distributions of neutron porosity increments in any well, or group of wells at one of the three sites, are zero-mean symmetric with heavy tails that decay with increasing vertical separation distance or lag. At all lags, the distributions are represented closely by either α-stable or normal-log-normal probability density models that tend to Gaussian with increasing lag. Both models represent scale mixtures of Gaussian variables with random variances that are, respectively, α-stable or log-normal.

3. Order q structure functions of absolute neutron porosity increments grow approximately as positive powers $\xi_w(q)$ of normalized lag, s_n, at $s_n < 10$ and as much

HESSD
11, 11637–11686, 2014

smaller positive powers, $\xi_b(q)$, of s_n at $s_n > 12$. We interpret this dual power-law scaling to represent within- or intra-layer variability at $s_n < 10$ and between- or inter-layer variability at $s_n > 12$. Values of $\xi_w(q = 1)$ and $\xi_b(q = 1)$ provide method-of-moment estimates of Hurst exponents H_w and H_b for these two power-law scaling ranges, respectively. Remarkably, a similar dual-scaling phenomenon has recently been reported by Siena et al. (2014) vis-a-vis porosities and specific surface areas imaged using x-ray computer micro-tomography throughout a millimeter-scale block of Estaillades limestone, at a spatial resolution of 3.3 µm, as well as Lagrangian velocities computed by solving the Stokes equation in the sample pore space.

4. Structure functions of absolute neutron porosity increments exhibit extended self similarity (ESS) at all normalized lags within both power-law scaling ranges, $s_n < 10$ and $s_n > 12$. Taking structure functions of order 1 to serve as reference, ESS provides another way to compute $\xi_w(q)$ and $\xi_b(q)$ for $q > 1$.

5. Values of power-law exponents $\xi_w(q)$ and $\xi_b(q)$ associated with absolute neutron porosity data, computed by the method of moments and by ESS, are for the most part very similar. Whereas such nonlinear scaling of power-law exponents has traditionally been viewed as a hallmark of multifractality (or, more recently, of fractional Laplace motion), we find the neutron porosity data in this paper to behave in a way fully consistent with that of samples from sub-Gaussian random fields subordinated to truncated (monofractal, self-affine, Gaussian) fractional Brownian motion or fractional Gaussian noise. The latter is the only view known to be theoretically consistent with ESS in the case of data, such as those considered here, that do not necessarily satisfy Burger's equation.

6. Our method of interpretation allows one to fully characterize the sub-Gaussian random field that underlies a given set of data by estimating the parameters of corresponding (generally truncated) power variograms, equivalent to semi-structure functions of second order.

HESSD
11, 11637–11686, 2014

7. The autocorrelation of neutron porosity increments diminishes rapidly with the number, n, of non-overlapping increments in a separation distance (lag). This helps explain why sample distributions of peaks over thresholds (POTs, taken here to be absolute increments which exceed their 95 % quantile) are described reasonably well by a generalized Pareto distribution (GPD) model, which in theory applies to independent identically distributed (iid) extrema. Whereas GPD shape parameter estimates do not show systematic variations with lag except in one well, corresponding estimates of GPD scale parameters tend to increase as a power of small lags and stabilize at larger lags. The same happens with scale parameters of α-stable distributions fitted to all (unfiltered) neutron porosity increments.

8. In all other respects, POTs show statistical scaling very similar to that of unfiltered increments. Estimates of POT Hurst exponents are very close to those obtained for unfiltered increments, with the exception of $\hat{H}_b$ that are consistently lower than those associated with unfiltered increments. Such nonlinear scaling is consistent with our method of interpreting the data.

Appendix A:

Let $\Delta Y = W^{1/2}\Delta G$ where $W^{1/2}$ is a random variable with probability density function (pdf) $f_W(w)$, and ΔG is a zero-mean Gaussian random field of increments with pdf $f_{\Delta G}(\Delta g)$ and variance $\sigma^2_{\Delta G}$ dependent on lag, ΔG and $W^{1/2}$ being statistically independent of each other at all lags. In this paper we consider $W^{1/2}$ to be either Lévy stable or lognormal. In the first case (e.g., Samorodnitsky and Taqqu, 1994) W is $\alpha/2$-stable totally skewed to the right of zero (hence non-negative) with scale parameter $\sigma_S = \left(\cos\frac{\pi\alpha}{4}\right)^{2/\alpha}$, unit skewness and zero shift. The corresponding pdf of ΔY is symmetric α-stable with zero skewness and shift. In the second case we follow Neuman (2011) and Guadagnini et al. (2012) by setting $W^{1/2} = e^V$ where V is zero-mean

HESSD
11, 11637–11686, 2014

Gaussian with variance $\sigma_V^2 = (2-\alpha)^2$, yielding the following respective mean and variance expressions for $W^{1/2}$,

$$\mu_W = \exp\left(\sigma_V^2/2\right) \quad \text{and} \quad \sigma_W^2 = \exp\left(\sigma_V^2\right)\left[\exp\left(\sigma_V^2\right) - 1\right]. \tag{A1}$$

Correspondingly, the pdf of ΔY is

$$f_{\Delta Y}(\Delta y) = \int_{-\infty}^{\infty} \frac{1}{|u|} f_U(u) f_{\Delta G}\left(\frac{\Delta y}{u}\right) \mathrm{d}u = \int_{-\infty}^{\infty} f_{\Delta Y|U}(\Delta y|u) f_U(u) \mathrm{d}u \tag{A2}$$

where $U = W^{1/2}$, $u = w^{1/2}$, $f_{\Delta Y|W^{1/2}}(\Delta y|w^{1/2}) = f_{\Delta Y|U}(\Delta y|u) = \frac{1}{|u|} f_{\Delta G}\left(\frac{\Delta y}{u}\right)$ is the conditional pdf of ΔY. Since $U = W^{1/2} > 0$ one has

$$f_{\Delta Y}(\Delta y) = \int_{0}^{\infty} \frac{1}{u} f_U(u) f_{\Delta G}\left(\frac{\Delta y}{u}\right) \mathrm{d}u. \tag{A3}$$

As $\Delta G \sim N(0, \sigma_{\Delta G}^2)$ and $U = W^{1/2} \sim \ln N(0, \sigma_V^2)$, Eq. (A3) becomes

$$f_{\Delta Y}(\Delta y|\sigma_{\Delta G}, \sigma_V) = \int_{0}^{\infty} \frac{1}{2\pi\sigma_V} \frac{1}{u^2} e^{-\frac{\Delta y^2}{2u^2}} \cdot e^{-\frac{(\ln u - \ln \sigma_{\Delta G})^2}{2\sigma_V^2}} \mathrm{d}u. \tag{A4}$$

This is the normal–log-normal (NLN) pdf we refer to in the text. In it $\sigma_{\Delta G}$ plays the role of a scale parameter, and σ_V of a shape factor. Letting $\sigma_V \to 0$ is tantamount to letting Eq. (A4) converge to a Normal density $f_{\Delta Y}(\Delta y|\sigma_{\Delta G}) = \frac{1}{\sqrt{2\pi}\sigma_{\Delta G}} e^{-\frac{(\Delta y)^2}{2\sigma_{\Delta G}^2}}$. The larger is σ_V the heavier are the tails and the sharper is the peak of the NLN distribution. Fitting Eq. (A4) by maximum likelihood (ML) to sample frequency distributions of ΔY allows one to estimate $\sigma_{\Delta G}^2$ and σ_V^2, which in turn allows one to estimate μ_W and σ_W^2 according to Eq. (A1).

HESSD
11, 11637–11686, 2014

Appendix B:

We set $\Delta Y(x, x+s) = W^{1/2}\Delta G(x, x+s)$ where x is a spatial (or temporal) coordinate, $s \geq 0$ is lag, $W^{1/2} = e^V$ independent of ΔG, V is zero-mean Gaussian with variance $\sigma_V^2 = (2-\alpha)^2$, and ΔG is a zero-mean second-order stationary random field of increments with variance $\sigma_{\Delta G}^2$ and covariance (or variogram) which depend on separation distance or lag. Clearly the mean of ΔY is zero. The 2nd-order raw moment of $W^{1/2}$ is

$$E[(W^{1/2})^2] = \mu_W^2 + \sigma_W^2 \tag{B1}$$

where $E[\,]$ denotes expectation and μ_W, σ_W^2 are defined in Eq. (A1). The variance of increments ΔY is $\sigma_{\Delta Y}^2 = \left(\mu_W^2 + \sigma_W^2\right)\sigma_{\Delta G}^2$ and the variogram of Y' is

$$\begin{aligned}\gamma_Y(s) &= \frac{1}{2}E[\Delta Y(x_1+s)\Delta Y(x_1+s)] = E[(W^{1/2})^2]E[\Delta G(x_1+s)\Delta G(x_1+s)] \\ &= \left(\sigma_W^2 + \mu_W^2\right)\gamma_G(s)\end{aligned} \tag{B2}$$

where $\gamma_G(s)$ is the variogram of G'. Once μ_W and σ_W^2 have been estimated by maximum likelihood on the basis of ΔY data as described in Appendix A, fitting Eq. (B2) to corresponding second-order sample structure functions allows one to estimate all parameters of $\gamma_G(s)$.

In case G' has a power variogram, $\gamma_G(s) = Bs^{2H}$, of the kind we consider in the manuscript so does Y,

$$\gamma_Y(s) = \left(\sigma_W^2 + \mu_W^2\right)\gamma_G(s) = Cs^{2H}, \tag{B3}$$

where C is a coefficient. Fitting Eq. (B3) to second-order sample structure functions of corresponding increments allows one to estimate C and H.

HESSD
11, 11637–11686, 2014

Acknowledgements. This work was supported in part through a contract between the University of Arizona and Vanderbilt University under the Consortium for Risk Evaluation with Stakeholder Participation (CRESP) III, funded by the US Department of Energy. Funding from MIUR (Italian ministry of Education, Universities and Research-PRIN2010-11; project: "Innovative methods for water resources under hydro-climatic uncertainty scenarios") is also acknowledged. We thank Muhammad Sahimi, University of Southern California, for having generously shared with us borehole geophysical log data some of which we analyze in this paper.

References

Akaev, A., Sadovnichy, V., and Korotayev, A.: On the dynamics of the world demographic transition and financial–economic crises forecasts, Eur. Phys. J.-Special Topics, 205, 355–373, doi:10.1140/epjst/e2012-01578-2, 2012.

Amitrano, D.: Variability in the power-law distributions of rupture events, Eur. Phys. J.-Special Topics, 205, 199–215, doi:10.1140/epjst/e2012-01571-9, 2012.

Ancey, C.: Are there "dragon-kings" events (i.e. genuine outliers) among extreme avalanches?, Eur. Phys. J.-Special Topics, 205, 117–129, doi:10.1140/epjst/e2012-01565-7, 2012.

Andrews, D. F. and Mallows, C. L.: Scale mixtures of normal distributions, J. Roy. Stat. Soc. B Met., 36, 99–102, 1974.

Barrash, W. and Reboulet, E. C.: Significance of porosity for stratigraphy and textural composition in subsurface coarse fluvial deposits, Boise Hydrogeophysical Research Site, Geol. Soc. Am. Bull., 116, 1059–1073, doi:10.1130/B25370.1, 2004.

Burlando, P. and Rosso, R.: Scaling and multiscaling models of depth–duration–frequency curves for storm precipitation, J. Hydrol., 187, 45–64, doi:10.1016/S0022-1694(96)03086-7, 1996.

Castro, J. J., Carsteanu, A. A., and Flores, C. G.: Intensity–duration–area–frequency functions for precipitation in a multi-fractal framework, Physica A, 338, 206–210, doi:10.1016/j.physa.2004.02.043, 2004.

Chakraborty, S., Frisch, U., and Ray, S. S.: Extended self-similarity works for the Burgers equation and why, J. Fluid Mech., 649, 275–285, doi:10.1017/S0022112010000595, 2010.

Dashtian, H., Jafari, G. R., Sahimi, M., and Masihi, M.: Scaling, multifractality, and long-range correlations in well log data of large-scale porous media, Physica A, 390, 2096–2111, doi:10.1016/j.physa.2011.01.010, 2011.

HESSD

11, 11637–11686, 2014

de Arcangelis, L.: Are dragon-king neuronal avalanches dungeons for self-organized brain activity?, Eur. Phys. J.-Special Topics, 205, 243–257, doi:10.1140/epjst/e2012-01574-6, 2012.
De Michele, C., Kottegoda, N. T., and Rosso, R.: The derivation of areal reduction factor of storm rainfall from its scaling properties, Water Resour. Res., 37, 3247–3252, doi:10.1029/2001WR000346, 2001.
Di Federico, V. and Neuman, S. P.: Scaling of random fields by means of truncated power variograms and associated spectra, Water Resour. Res., 33, 1075–1085, doi:10.1029/97WR00299, 1997.
Ebtehaj, M. and Foufoula-Georgiou, E.: Orographic signature on multiscale statistics of extreme rainfall: a storm-scale study, J. Geophys. Res.-Atmos., 115, D23112, doi:10.1029/2010JD014093, 2010.
Embrechts, P., Mikosch, T., and Klüppelberg, C.: Modelling Extremal Events for Insurance and Finance, Springer-Verlag, London, UK, 1997.
Fogg, G. E., Carle, S. F., and Green, C.: Connected-network paradigm for the alluvial aquifer system, in: Theory, Modeling, and Field Investigation in Hydrogeology: a Special Volume in Honor of Shlomo P. Neuman's 60th Birthday, edited by: Zhang, D. and Winter, C. L., Boulder, Colorado, Geol. S. Am. S., 348, 25–42, 2000.
Garcia-Bartual, R. and Schneider, M.: Estimating maximum expected short-duration rainfall intensities from extreme convective storms, Phys. Chem. Earth Pt. B, 26, 675–681, doi:10.1016/S1464-1909(01)00068-5, 2001.
Golosovsky, M. and Solomon, S.: Runaway events dominate the heavy tail of citation distributions, Eur. Phys. J.-Special Topics, 205, 303–311, doi:10.1140/epjst/e2012-01576-4, 2012.
Gómez-Hernández, J. J. and Wen, X.-H.: To be or not to be multi-Gaussian. A reflection on stochastic hydrogeology, Adv. Water Resour., 21, 47–61, doi:10.1016/S0309-1708(96)00031-0, 1998.
Guadagnini, A. and Neuman, S. P.: Extended power-law scaling of self-affine signals exhibiting apparent multifractality, Geophys. Res. Lett., 38, L13403, doi:10.1029/2011gl047727, 2011.
Guadagnini, A., Neuman, S. P., and Riva, M.: Numerical investigation of apparent multifractality of samples from processes subordinated to truncated fBm, Hydrol. Process., 26, 2894–2908, doi:10.1002/Hyp.8358, 2012.
Guadagnini, A., Neuman, S. P., Schaap, M. G., and Riva, M.: Anisotropic statistical scaling of vadose zone hydraulic property estimates near Maricopa, Arizona, Water Resour. Res., 49, 8463–8479, doi:10.1002/2013wr014286, 2013.

HESSD
11, 11637–11686, 2014

Guadagnini, A., Neuman, S. P., Schaap, M. G., and Riva, M.: Anisotropic statistical scaling of soil and sediment texture in a stratified deep vadose zone near Maricopa, Arizona, Geoderma, 214, 217–227, doi:10.1016/j.geoderma.2013.09.008, 2014.

Janczura, J. and Weron, R.: Black swans or dragon-kings? A simple test for deviations from the power law, Eur. Phys. J.-Special Topics, 205, 79–93, doi:10.1140/epjst/e2012-01563-9, 2012.

Javelle, P., Gresillon, J. M., and Galea, G.: Discharge–duration–frequency curve modelling for floods and scale invariance, CR Acad. Sci. II A, 329, 39–44, doi:10.1016/S1251-8050(99)80225-0, 1999.

Kashyap, R. L.: Optimal choice of AR and MA parts in autoregressive moving average models, IEEE T. Pattern Anal., 4, 99–104, 1982.

Katz, R. W., Parlange, M. B., and Naveau, P.: Statistics of extremes in hydrology, Adv. Water Resour., 25, 1287–1304, doi:10.1016/S0309-1708(02)00056-8, 2002.

Knudby, C. and Carrera, J.: On the relationship between indicators of geostatistical, flow and transport connectivity, Adv. Water Resour., 28, 405–421, doi:10.1016/j.advwatres.2004.09.001, 2005.

Knudby, C. and Carrera, J.: On the use of apparent hydraulic diffusivity as an indicator of connectivity, J. Hydrol., 329, 377–389, doi:10.1016/j.jhydrol.2006.02.026, 2006.

Knudby, C., Carrera, J., Bumgardner, J. D., and Fogg, G. E.: Binary upscaling – the role of connectivity and a new formula, Adv. Water Resour., 29, 590–604, 2006.

Langousis, A. and Veneziano, D.: Intensity–duration–frequency curves from scaling representations of rainfall, Water Resour. Res., 43, W02422, doi:10.1029/2006wr005245, 2007.

Lei, X.: Dragon-Kings in rock fracturing: insights gained from rock fracture tests in the laboratory, Eur. Phys. J.-Special Topics, 205, 217–230, doi:10.1140/epjst/e2012-01572-8, 2012.

Main, I. and Naylor, M.: Extreme events and predictability of catastrophic failure in composite materials and in the Earth, Eur. Phys. J.-Special Topics, 205, 183–197, doi:10.1140/epjst/e2012-01570-x, 2012.

Mariethoz, G. and Renard, P.: Special Issues on 20 years of multiple-point statistics: part 2, Math. Geosci., 46, 517–518, doi:10.1007/s11004-014-9545-y, 2014.

Meier, P. M., Carrera, J., and Sanchez-Vila, X.: An evaluation of Jacob's method for the interpretation of pumping tests in heterogeneous formations, Water Resour. Res., 34, 1011–1025, doi:10.1029/98WR00008, 1998.

HESSD
11, 11637–11686, 2014

Menabde, M. and Sivapalan, M.: Linking space–time variability of river runoff and rainfall fields: a dynamic approach, Adv. Water Resour., 24, 1001–1014, doi:10.1016/S0309-1708(01)00038-0, 2001.
Menabde, M., Seed, A., and Pegram, G.: A simple scaling model for extreme rainfall, Water Resour. Res., 35, 335–339, doi:10.1029/1998wr900012, 1999.
Mohymont, B. and Demarée, G. R.: Intensity–duration–frequency curves for precipitation at Yangambi, Congo, derived by means of various models of Montana type, Hydrolog. Sci. J., 51, 239–253, doi:10.1623/hysj.51.2.239, 2006.
Neuman, S. P.: Apparent/spurious multifractality of absolute increments sampled from truncated fractional Gaussian/Levy noise, Geophys. Res. Lett., 37, L09403, doi:10.1029/2010gl043314, 2010.
Neuman, S. P.: Apparent multifractality and scale-dependent distribution of data sampled from self-affine processes, Hydrol. Process., 25, 1837–1840, doi:10.1002/Hyp.7967, 2011.
Neuman, S. P., Guadagnini, A., Riva, M., and Siena, M.: Recent advances in statistical and scaling analysis of earth and environmental variables, in: Advances in Hydrogeology, edited by: Mishra, P. K. and Kuhlman, K. L., Springer, New York, 2013.
Nguyen, V. T. V., Nguyen, T. D., and Wang, H.: Regional estimation of short duration rainfall extremes, Water Sci. Technol., 37, 15–19, doi:10.1016/S0273-1223(98)00311-4, 1998.
Nield, D. A.: Connectivity and effective hydraulic conductivity, Transport Porous Med., 74, 129–132, doi:10.1007/s11242-007-9185-5, 2008.
Nolan, J.: Maximum likelihood estimation of stable parameters, in: Lévy Processes: Theory and Applications, edited by: Barndorff-Nielsen, O., Mikosch, T., and Resnick, S., Birkhauser, Boston, 2001.
Pisarenko, V. F. and Sornette, D.: Robust statistical tests of Dragon-Kings beyond power law distributions, Eur. Phys. J.-Special Topics, 205, 95–115, doi:10.1140/epjst/e2012-01564-8, 2012.
Plenz, D.: Neuronal avalanches and coherence potentials, Eur. Phys. J.-Special Topics, 205, 259–301, doi:10.1140/epjst/e2012-01575-5, 2012.
Renard, P. and Mariethoz, G.: Special Issues on 20 years of multiple-point statistics: part 1, Math. Geosci., 46, 129–131, doi:10.1007/s11004-014-9524-3, 2014.
Rigon, R., D'Odorico, P., and Bertoldi, G.: The geomorphic structure of the runoff peak, Hydrol. Earth Syst. Sci., 15, 1853–1863, doi:10.5194/hess-15-1853-2011, 2011.

HESSD
11, 11637–11686, 2014

Riva, M., Neuman, S. P., and Guadagnini, A.: On the identification of Dragon Kings among extreme-valued outliers, Nonlin. Processes Geophys., 20, 549–561, doi:10.5194/npg-20-549-2013, 2013a.
Riva, M., Neuman, S. P., Guadagnini, A., and Siena, M.: Anisotropic scaling of berea sandstone log air permeability statistics, Vadose Zone J., 12, 1–15, doi:10.2136/Vzj2012.0153, 2013b.
Riva, M., Neuman, S. P., and Guadagnini, A.: Sub-Gaussian model of processes with heavy-tailed distributions applied to air permeabilities of fractured tuff, Stoch. Env. Res. Risk A., 27, 195–207, doi:10.1007/s00477-012-0576-y, 2013c.
Riva, M., Sanchez-Vila, X., and Guadagnini, A.: Estimation of spatial covariance of log conductivity from particle size data, Water Resour. Res., 50, 5298–5308, doi:10.1002/2014WR015566, 2014.
Sachs, M., Yoder, M., Turcotte, D., Rundle, J., and Malamud, B.: Black swans, power laws, and dragon-kings: earthquakes, volcanic eruptions, landslides, wildfires, floods, and SOC models, Eur. Phys. J.-Special Topics, 205, 167–182, doi:10.1140/epjst/e2012-01569-3, 2012.
Samorodnitsky, G. and Taqqu, M. S.: Stable Non-Gaussian Random Processes, Chapman and Hall, New York, 1994.
Sanchez-Vila, X., Carrera, J., and Girardi, J. P.: Scale effects in transmissivity, J. Hydrol., 183, 1–22, doi:10.1016/S0022-1694(96)80031-X, 1996.
Schertzer, D. and Lovejoy, S.: Physical modeling and analysis of rain and clouds by anisotropic scaling multiplicative processes, J. Geophys. Res.-Atmos., 92, 9693–9714, doi:10.1029/Jd092id08p09693, 1987.
Schoenberg, F. and Patel, R.: Comparison of Pareto and tapered Pareto distributions for environmental phenomena, Eur. Phys. J.-Special Topics, 205, 159–166, doi:10.1140/epjst/e2012-01568-4, 2012.
Siena, M., Guadagnini, A., Riva, M., and Neuman, S. P.: Extended power-law scaling of air permeabilities measured on a block of tuff, Hydrol. Earth Syst. Sci., 16, 29–42, doi:10.5194/hess-16-29-2012, 2012.
Siena, M., Guadagnini, A., Riva, M., Bijeljic, B., Pereira Nunes, J. P., and Blunt, M. J.: Statistical scaling of pore-scale Lagrangian velocities in natural porous media, Phys. Rev. E, 90, 023013, doi:10.1103/PhysRevE.90.023013, 2014.
Süveges, M. and Davison, A.: A case study of a “Dragon-King”: the 1999 Venezuelan catastrophe, Eur. Phys. J.-Special Topics, 205, 131–146, doi:10.1140/epjst/e2012-01566-6, 2012.

HESSD
11, 11637–11686, 2014

Trefry, C. M., Watkins, D. W., and Johnson, D.: Regional rainfall frequency analysis for the state of Michigan, J. Hydrol. Eng., 10, 437–449, doi:10.1061/(Asce)1084-0699(2005)10:6(437), 2005.

Tronicke, J. and Holliger, K.: Quantitative integration of hydrogeophysical data: conditional geostatistical simulation for characterizing heterogeneous alluvial aquifers, Geophysics, 70, H1–H10, doi:10.1190/1.1925744, 2005.

Veneziano, D. and Furcolo, P.: Multifractality of rainfall and scaling of intensity–duration–frequency curves, Water Resour. Res., 38, 1306, doi:10.1029/2001WR000372, 2002.

Veneziano, D. and Yoon, S.: Rainfall extremes, excesses, and intensity-duration-frequency curves: a unified asymptotic framework and new nonasymptotic results based on multifractal measures, Water Resour. Res., 49, 4320–4334, doi:10.1002/wrcr.20352, 2013.

Veneziano, D., Langousis, A., and Lepore, C.: New asymptotic and preasymptotic results on rainfall maxima from multifractal theory, Water Resour. Res., 45, W11421, doi:10.1029/2009wr008257, 2009.

Vuković, M. and Soro, A.: Determination of Hydraulic Conductivity of Porous Media from Grain-Size Composition, Water Resources Publications, Littleton, Colorado, 1992.

Wen, X.-H. and Gómez-Hernández, J. J.: Numerical modeling of macrodispersion in heterogeneous media – a comparison of multi-Gaussian and non-multi-Gaussian models, J. Contam. Hydrol., 30, 129–156, doi:10.1016/S0169-7722(97)00035-1, 1998.

West, M.: On scale mixtures of normal distributions, Biometrika, 74, 646–648, doi:10.1093/biomet/74.3.646, 1987.

Western, A. W., Blöschl, G., and Grayson, R. B.: Toward capturing hydrologically significant connectivity in spatial patterns, Water Resour. Res., 37, 83–97, doi:10.1029/2000WR900241, 2001.

Willems, P.: Compound intensity/duration/frequency-relationships of extreme precipitation for two seasons and two storm types, J. Hydrol., 233, 189–205, doi:10.1016/S0022-1694(00)00233-X, 2000.

Yu, P. S., Yang, T. C., and Lin, C. S.: Regional rainfall intensity formulas based on scaling property of rainfall, J. Hydrol., 295, 108–123, doi:10.1016/j.jhydrol.2004.03.003, 2004.

Zinn, B. and Harvey, C. F.: When good statistical models of aquifer heterogeneity go bad: a comparison of flow, dispersion, and mass transfer in connected and multivariate Gaussian hydraulic conductivity fields, Water Resour. Res., 39, 1051, doi:10.1029/2001WR001146, 2003.

HESSD

11, 11637–11686, 2014

Table 1. Summary information about available neutron porosity (P) data.

Reservoir	Well #	Sampling interval (m)	Min P (%)	Max P (%)	Mean P (%)	Standard Deviation SD (%)	Number of data points used
Maroon (MN)	1	0.1524	0	46.04	14	6.4	3567
	2	0.1524	0[a]	74.29	17.27	9.98	4049
	3	0.1524	0[a]	37.6	15.72	8.54	2945
	1 + 2 + 3	0.1524	0[a]	74.29	15.74	8.62	10 561
Ahwaz (AZ)	4	0.1524	0	36.01	16.47	6.82	3882
	5	0.1524	0	47.91	16.05	8.35	6949
Tabnak (TBK)	6	0.0762[b]	0	96.9	9.28	13.2	4267

[a] These, being negative and very close to zero, were set equal to zero.
[b] We disregard every other measurement in analyzing these data.

HESSD
11, 11637–11686, 2014

Table 2. Method of moments estimates of H for porosity increments at $s_n < 10$ (denoted by subscript w) and $s_n > 12$ (subscript b).

Well	$\hat{H}_w$	$\hat{H}_b$
1 (Maroon field)	0.86	0.10
2 (Maroon field)	0.87	0.08
3 (Maroon field)	0.85	0.11
4 (Ahwaz field)	0.70	0.11
5 (Ahwaz field)	0.66	0.16
6 (Tabnak field)	0.75	0.17

HESSD
11, 11637–11686, 2014

Table 3. Estimates $\hat{A}$ of A given estimates $\hat{H}$ of H from Table 2, and joint estimates $\hat{A}$ and $\hat{H}$, of PVs with associated 95 % confidence limits (in parenthesis) for all wells at $s_n < 10$ and $s_n > 12$ in the case of α-stable subordinator.

Data source	$\hat{A}$ estimated using $\hat{H}$ from Table 2		Joint estimates $\hat{A}$ and $\hat{H}$	
	$\hat{H}$	$\hat{A}$	$\hat{H}$	$\hat{A}$
Well 1 $s_n < 10$	0.86	0.06 (0.05; 0.07)	0.87 (0.78; 0.97)	0.05 (0.02; 0.13)
Well 1 $s_n > 12$	0.10	2.12 (1.84; 2.45)	0.14 (0.10; 0.20)	2.00 (1.66; 2.43)
Well 2 $s_n < 10$	0.87	0.12 (0.11; 0.13)	0.91 (0.86; 0.96)	0.08 (0.04; 0.16)
Well 2 $s_n > 12$	0.08	5.14 (4.48; 5.90)	0.10 (0.06; 0.16)	5.27 (4.56; 6.08)
Well 3 $s_n < 10$	0.85	0.16 (0.14; 0.17)	0.89 (0.82 0.96)	0.11 (0.05; 0.23)
Well 3 $s_n > 12$	0.11	4.02 (3.60; 4.49)	0.09 (0.06; 0.14)	4.02 (3.59; 4.51)
Well 4 $s_n < 10$	0.70	0.21 (0.19; 0.24)	0.76 (0.70; 0.83)	0.16 (0.11; 0.23)
Well 4 $s_n > 12$	0.11	1.80 (1.67; 1.94)	0.13 (0.11; 0.16)	1.74 (1.59; 1.90)
Well 5 $s_n < 10$	0.66	0.18 (0.15; 0.23)	0.70 (0.53; 0.93)	0.15 (0.06; 0.37)
Well 5 $s_n > 12$	0.16	1.36 (1.13; 1.65)	0.25 (0.22; 0.30)	0.84 (0.64; 1.11)
Well 6 $s_n < 10$	0.75	0.09 (0.08; 0.11)	0.81 (0.70; 0.94)	0.06 (0.03; 0.14)
Well 6 $s_n > 12$	0.17	0.86 (0.78; 0.94)	0.18 (0.15; 0.22)	0.80 (0.66; 0.96)

HESSD
11, 11637–11686, 2014

Table 4. Estimates $\hat{C}$ of C given estimates $\hat{H}$ of H from Table 2, and joint estimates $\hat{C}$ and $\hat{H}$, of PVs with associated 95 % confidence limits (in parenthesis) for all wells at $s_n < 10$ and $s_n > 12$ in the case of lognormal subordinator.

Data source	$\hat{C}$ estimated using $\hat{H}$ from Table 2		Joint estimates $\hat{C}$ and $\hat{H}$	
	$\hat{H}$	$\hat{C}$	$\hat{H}$	$\hat{C}$
Well 1 $s_n < 10$	0.86	0.52 (0.46; 0.58)	0.85 (0.75; 0.96)	0.53 (0.40; 0.70)
Well 1 $s_n > 12$	0.10	13.22 (12.36; 14.13)	0.07 (0.05; 0.08)	17.88 (15.44; 20.70)
Well 2 $s_n < 10$	0.87	1.35 (1.18; 1.53)	0.84 (0.74; 0.96)	1.43 (1.07; 1.92)
Well 2 $s_n > 12$	0.08	39.31 (36.17; 42.72)	0.04 (0.03; 0.07)	55.61 (45.31; 68.24)
Well 3 $s_n < 10$	0.85	0.87 (0.76; 1.00)	0.83 (0.72; 0.95)	0.91 (0.67; 1.25)
Well 3 $s_n > 12$	0.11	19.96 (18.30; 21.77)	0.09 (0.06; 0.12)	24.88 (18.72; 33.06)
Well 4 $s_n < 10$	0.70	1.09 (0.92; 1.31)	0.65 (0.52; 0.80)	1.23 (0.85; 1.80)
Well 4 $s_n > 12$	0.11	10.02 (9.48; 10.59)	0.08 (0.07; 0.09)	13.01 (11.66; 14.52)
Well 5 $s_n < 10$	0.66	1.59 (1.35; 1.88)	0.61 (0.50; 0.75)	1.78 (1.25; 2.53)
Well 5 $s_n > 12$	0.16	8.69 (7.73; 9.76)	0.09 (0.08; 0.11)	16.05 (13.83; 18.61)
Well 6 $s_n < 10$	0.76	2.52 (2.15; 2.95)	0.71 (0.60; 0.84)	2.77 (1.98; 3.89)
Well 6 $s_n > 12$	0.17	26.90 (24.45; 29.58)	0.14 (0.11; 0.17)	37.02 (27.90; 49.11)

HESSD
11, 11637–11686, 2014

Table 5. POT sample sizes and Kolmogorov–Smirnov p values associated with three lags in various wells.

s_n	Well No.	No. of samples	No. of POT samples	p value (KS test)
1	1	3566	177	0.240
	2	4048	202	0.994
	3	2944	147	0.706
	4	3881	194	0.437
	5	6948	208	0.970
	6	4265	213	0.788
32	1	3535	177	0.612
	2	4017	201	0.199
	3	2913	146	0.394
	4	3850	191	0.426
	5	6917	208	0.313
	6	4203	210	0.215
1024	1	2543	126	0.089
	2	3025	151	0.530
	3	1921	96	0.928
	4	2858	143	0.473
	5	5925	178	0.072
	6	2219	111	0.590

HESSD
11, 11637–11686, 2014

Table 6. Method of moments estimates of H for POTs at $s_n < 10$ (denoted by subscript w) and $s_n > 12$ (subscript b).

Well	$\hat{H}_w$	$\hat{H}_b$
1 (Maroon field)	0.84	0.02
2 (Maroon field)	0.83	0.0001
3 (Maroon field)	0.80	0.06
4 (Ahwaz field)	0.61	0.03
5 (Ahwaz field)	0.60	0.02
6 (Tabnak field)	0.71	0.11

HESSD
11, 11637–11686, 2014

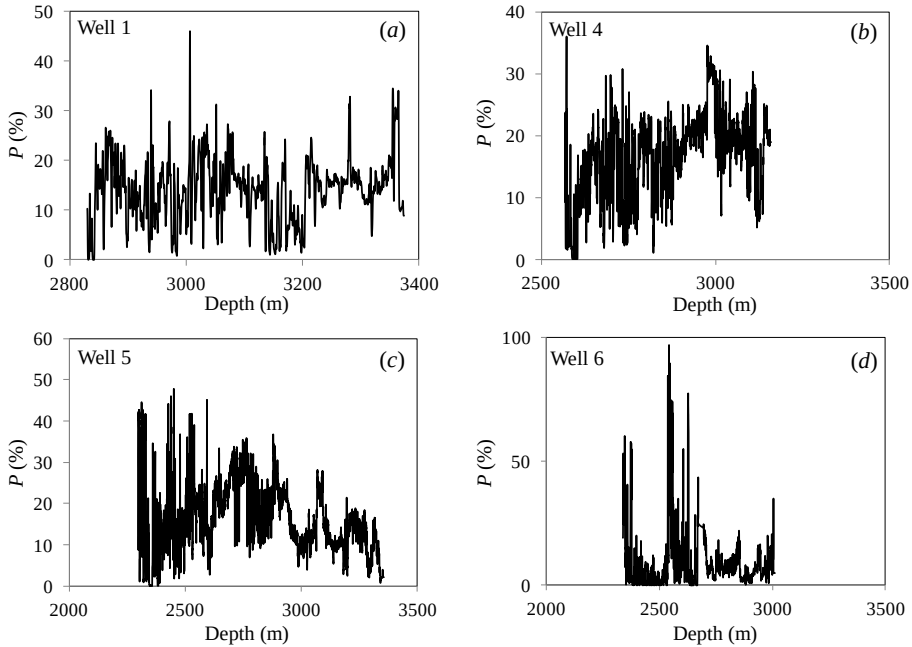

Figure 1. Variation of neutron porosity (P) with depth in Wells 1 (Maroon field), 4–5 (Ahwaz field) and 6 (Tabnak field).

HESSD
11, 11637–11686, 2014

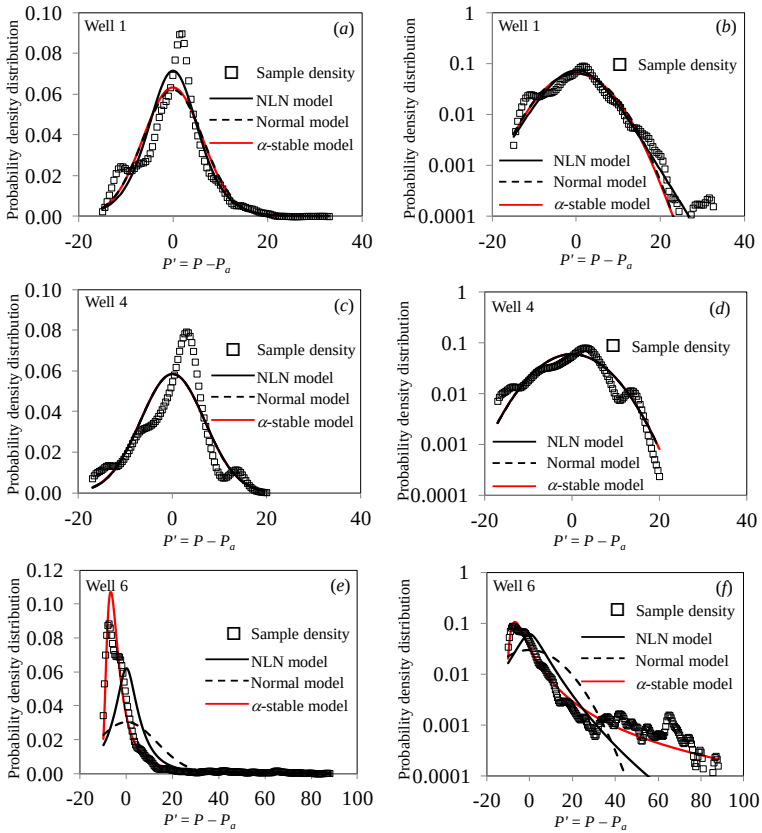

Figure 2. Frequency distributions on arithmetic and semi-logarithmic scales of $P' = P - P_a$ in **(a, b)** Well 1 (Maroon field), **(c, d)** Well 4 (Ahwaz field), and **(e, f)** Well 6 (Tabnak field). Also shown are ML fits of Gaussian (dashed), α-stable (solid red), and NLN (black solid) pdfs.

HESSD
11, 11637–11686, 2014

CC BY

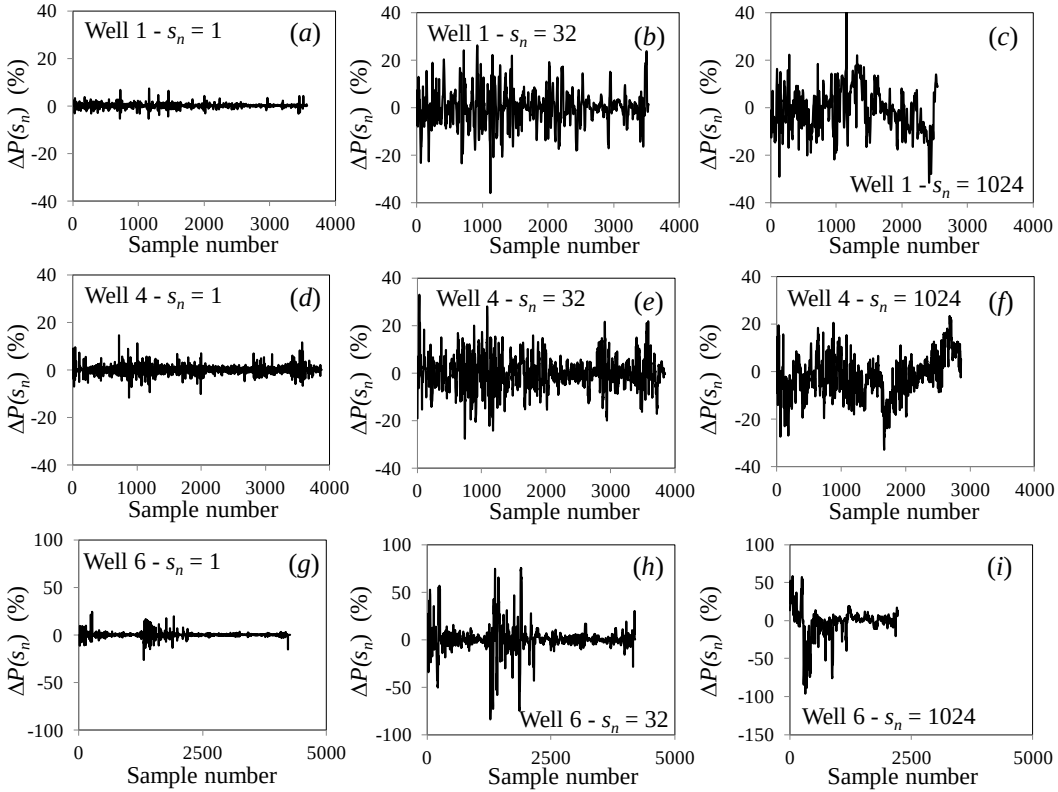

Figure 3. Increments $\Delta P(s_n)$ of P at normalized lags $s_n = 1$ ($s = 0.15$ m), 32 ($s = 4.80$ m), and 1024 ($s = 153.60$ m) vs. sequential (integer) vertical position in **(a)–(c)** Well 1 (Maroon field), **(d)–(f)** Well 4 (Ahwaz field), and **(g)–(i)** Well 6 (Tabnak field).

HESSD
11, 11637–11686, 2014

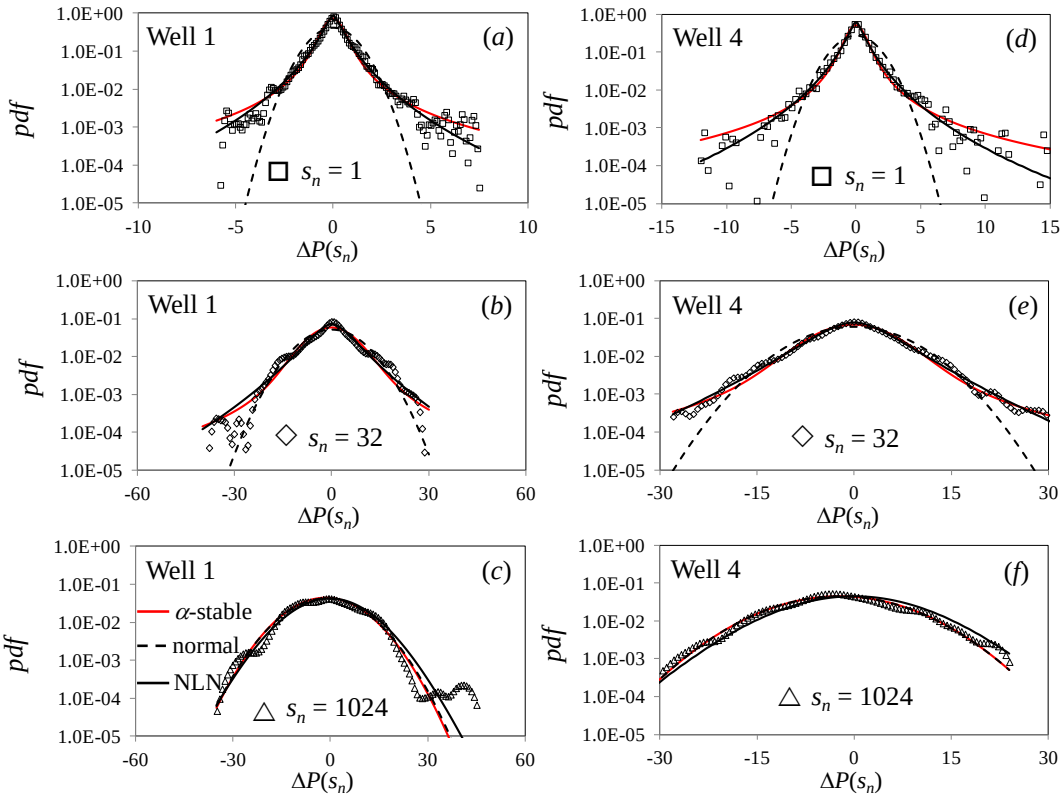

Figure 4. Frequency distributions of increments $\Delta P(s_n)$ of P at normalized lags $s_n = 1$ (s = 0.15 m), 32 (s = 4.80 m), and 1024 (s = 153.60 m) in **(a)–(c)** Well 1 (Maroon field) and **(d)–(f)** Well 4 (Ahwaz field). Also shown are ML fits of Gaussian (dashed), α-stable (solid red), and NLN (black solid) pdfs.

HESSD
11, 11637–11686, 2014

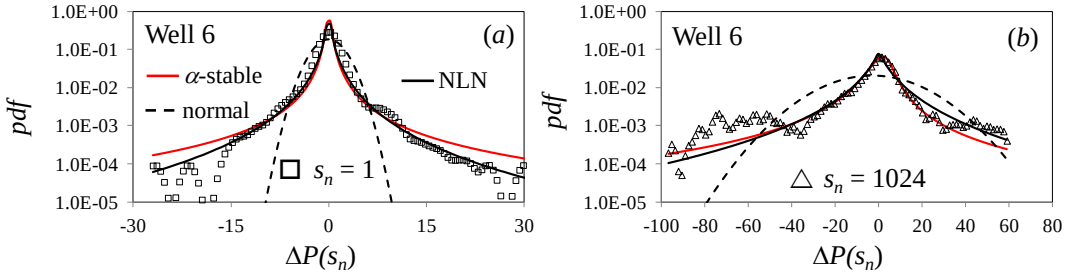

Figure 5. Frequency distributions of increments $\Delta P(s_n)$ of P at normalized lags $s_n = 1$ (s = 0.15 m) and 1024 (s = 153.60 m) in Well 6 (Tabnak field). Also shown are ML fits of Gaussian (dashed), α-stable (solid red), and NLN (black solid) pdfs.

HESSD
11, 11637–11686, 2014

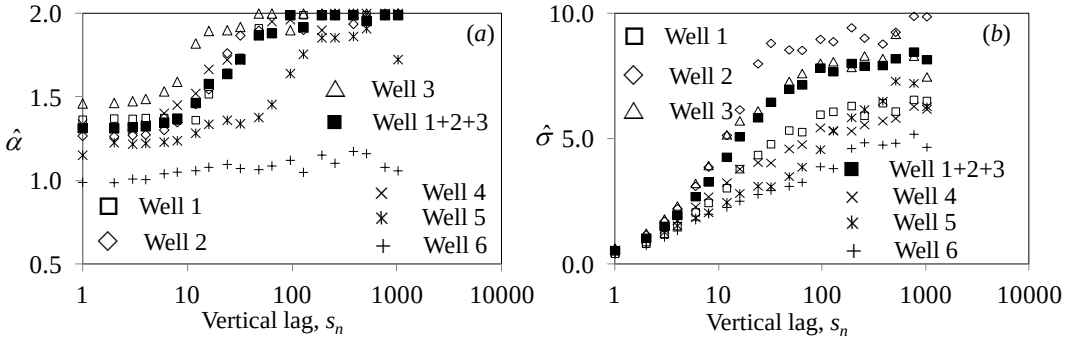

Figure 6. ML estimates $\hat{\alpha}$ and $\hat{\sigma}$ of stability and scale parameters, respectively, characterizing α-stable distribution models of increments $\Delta P(s_n)$ of P in all wells vs. normalized lag.

HESSD
11, 11637–11686, 2014

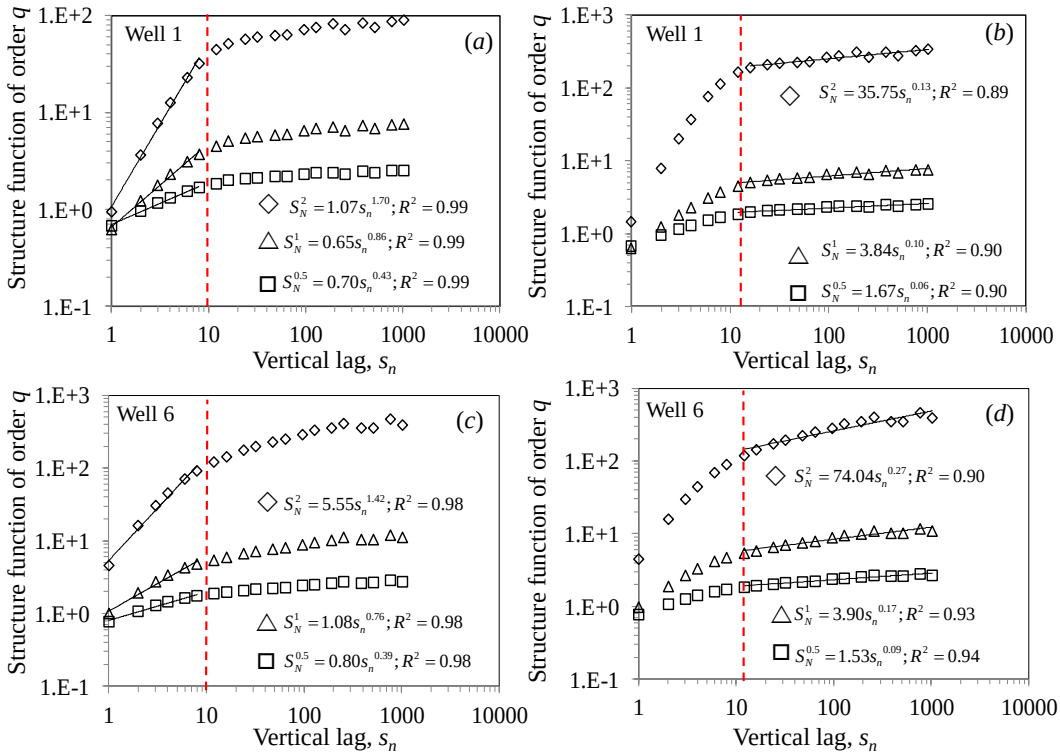

Figure 7. $S_N^q(s_n)$ vs. normalized lag for q = 0.5, 1.0, and 2.0 in Wells 1 (Maroon) and 6 (Tabnak). Red dashed line demarcates breaks in power-law scaling regimes. Logarithmic scale regression lines and corresponding power-law relations between $S_N^q(s_n)$ and s_n are given in **(a)** for Well 1 at $s_n < 10$, **(b)** Well 1 at $s_n > 12$, **(c)** Well 6 at $s_n < 10$, and **(d)** Well 6 at $s_n > 12$.

HESSD
11, 11637–11686, 2014

Extreme value statistics of scalable data exemplified by neutron porosities in deep boreholes

A. Guadagnini et al.

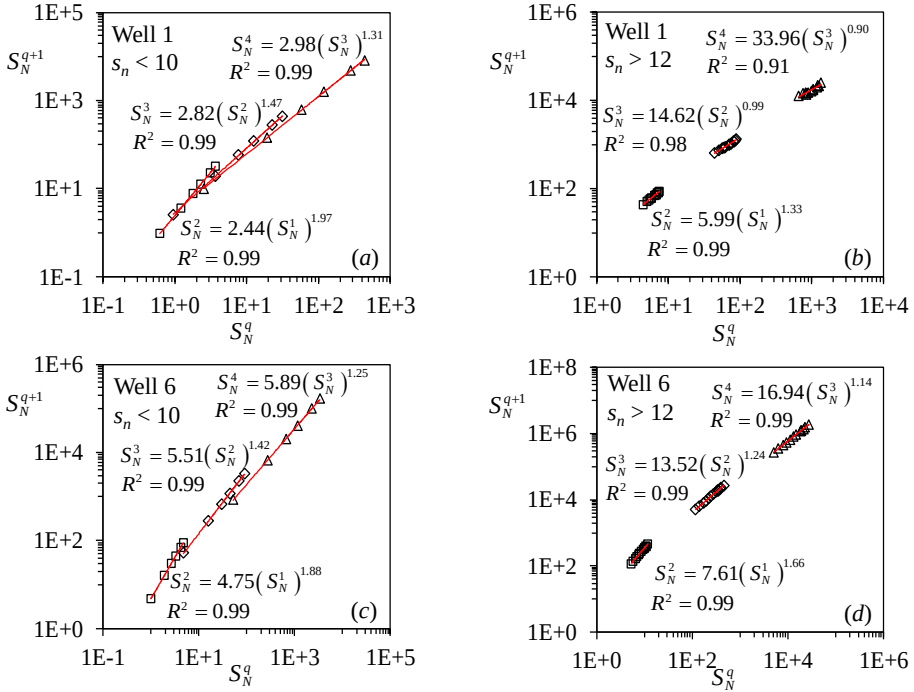

Figure 8. S_N^{q+1} vs. S_N^q for q = 1, 2 and 3 in Wells 1 (Maroon) and 6 (Tabnak). Logarithmic scale regression lines and corresponding power-law relations between S_N^{q+1} vs. S_N^q are given in **(a)** for Well 1 at $s_n < 10$, **(b)** Well 1 at $s_n > 12$, **(c)** Well 6 at $s_n < 10$, and **(d)** Well 6 at $s_n > 12$.

HESSD
11, 11637–11686, 2014

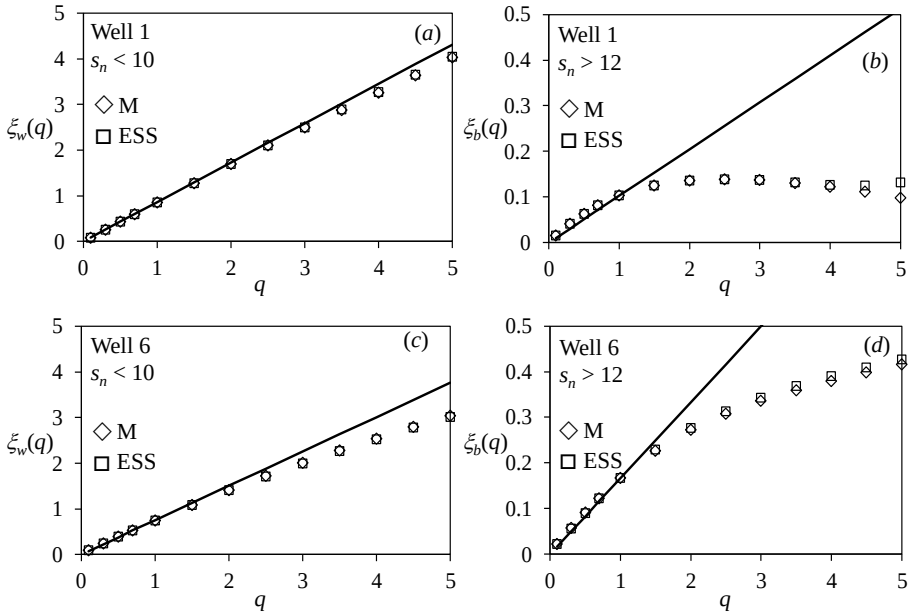

Figure 9. $\xi_w(q)$ and $\xi_b(q)$ evaluated as functions of q by the method of moments (M) and ESS in **(a)** Well 1 at $s_n < 10$, **(b)** Well 1 at $s_n > 12$, **(c)** Well 6 at $s_n < 10$, and **(d)** Well 6 at $s_n > 12$.

HESSD
11, 11637–11686, 2014

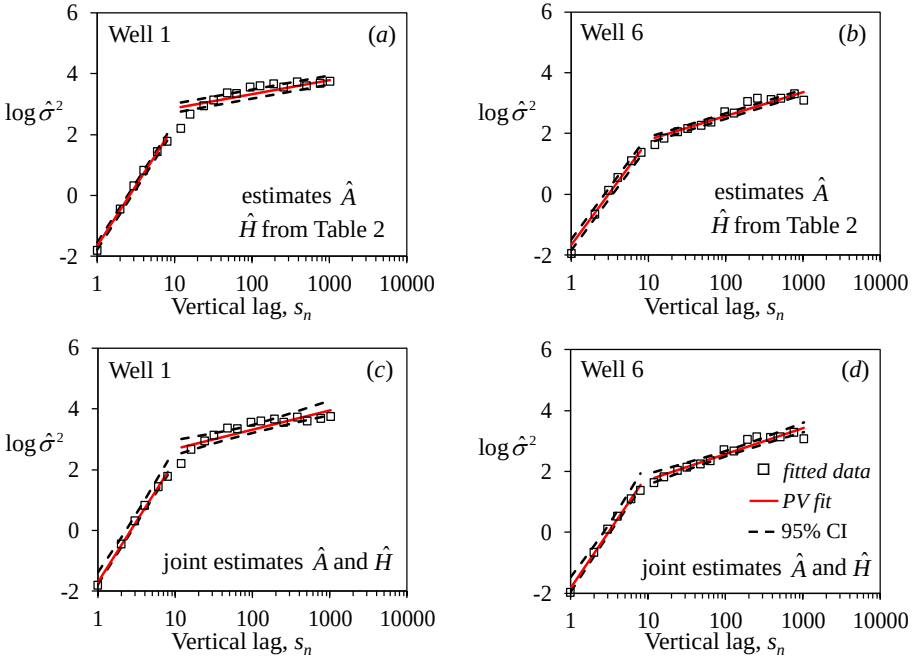

Figure 10. Sample scale parameter drop $\hat{\sigma}^2(s_n)$ as functions of s_n (squares), ML fitted PVs (solid lines) and 95 % confidence limits (broken curves) in Wells 1 and 6 based on **(a, b)** estimates $\hat{A}$ given estimates $\hat{H}$ from Table 2 and **(c, d)** joint estimates of $\hat{A}$ and $\hat{H}$.

HESSD
11, 11637–11686, 2014

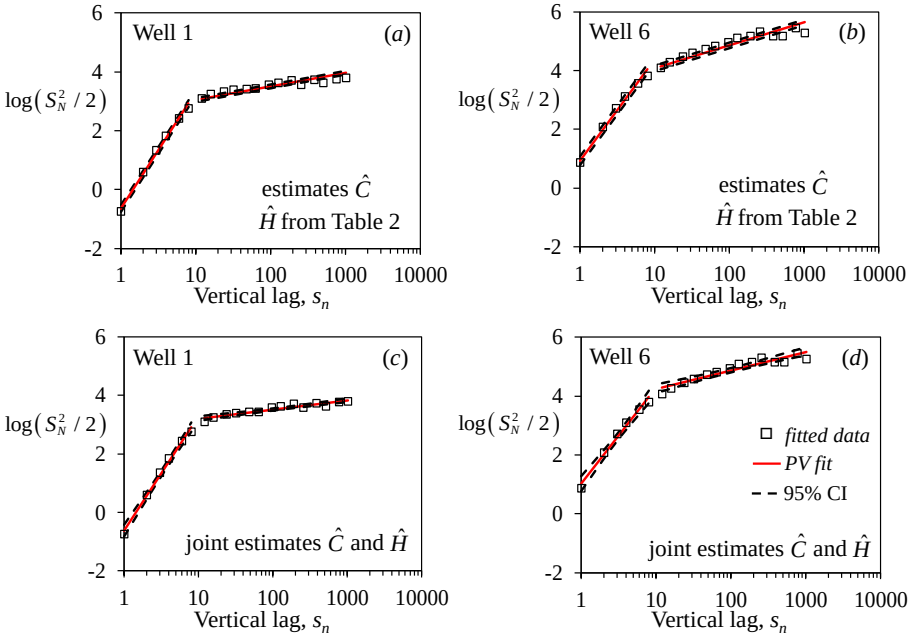

Figure 11. Sample structure functions, $S_N^2(s_n)$, of order $q = 2$ as functions of s_n (squares), ML fitted PVs (solid lines) and 95 % confidence limits (broken curves) in Wells 1 and 6 based on **(a, b)** estimates $\hat{C}$ given estimates $\hat{H}$ from Table 2 and **(c, d)** joint estimates of $\hat{C}$ and $\hat{H}$.

HESSD
11, 11637–11686, 2014

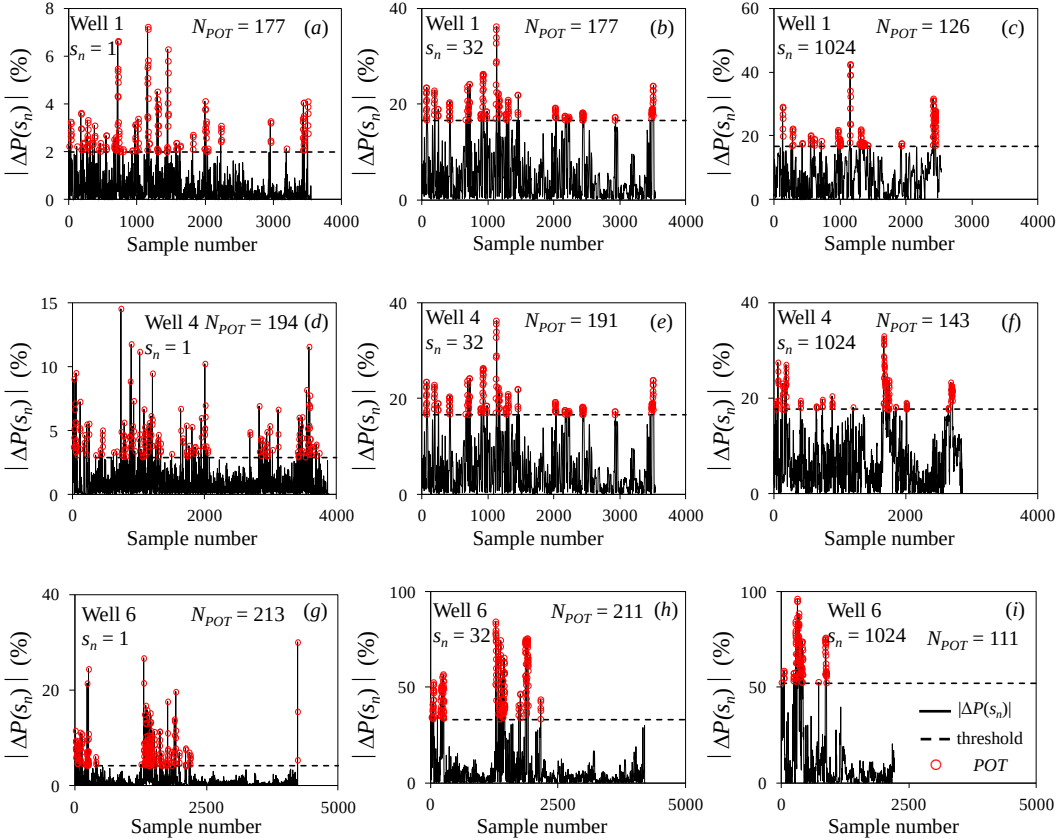

Figure 12. POTs of absolute increments $|\Delta P(s_n)|$ at normalized lags s_n = 1, 32, and 1024 vs. sequential (integer) vertical position in **(a)–(c)** Well 1 (Maroon), **(d)–(f)** Well 4 (Ahwaz), and **(g)–(i)** Well 6 (Tabnak).

HESSD
11, 11637–11686, 2014

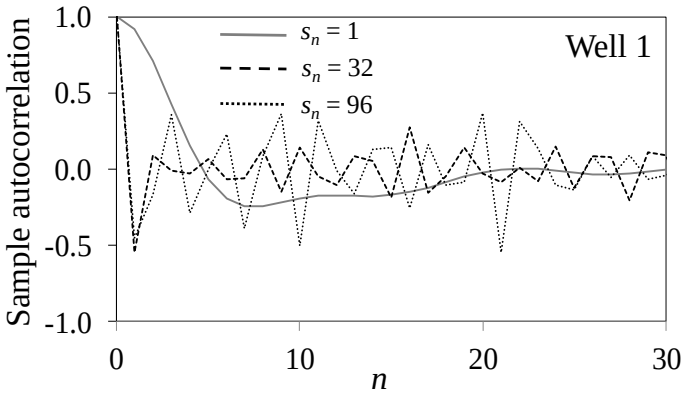

Figure 13. Sample autocorrelations of neutron porosity increments at normalized lags $s_n = 1$, 32 and 96 in Well 1 as functions of n.

HESSD
11, 11637–11686, 2014

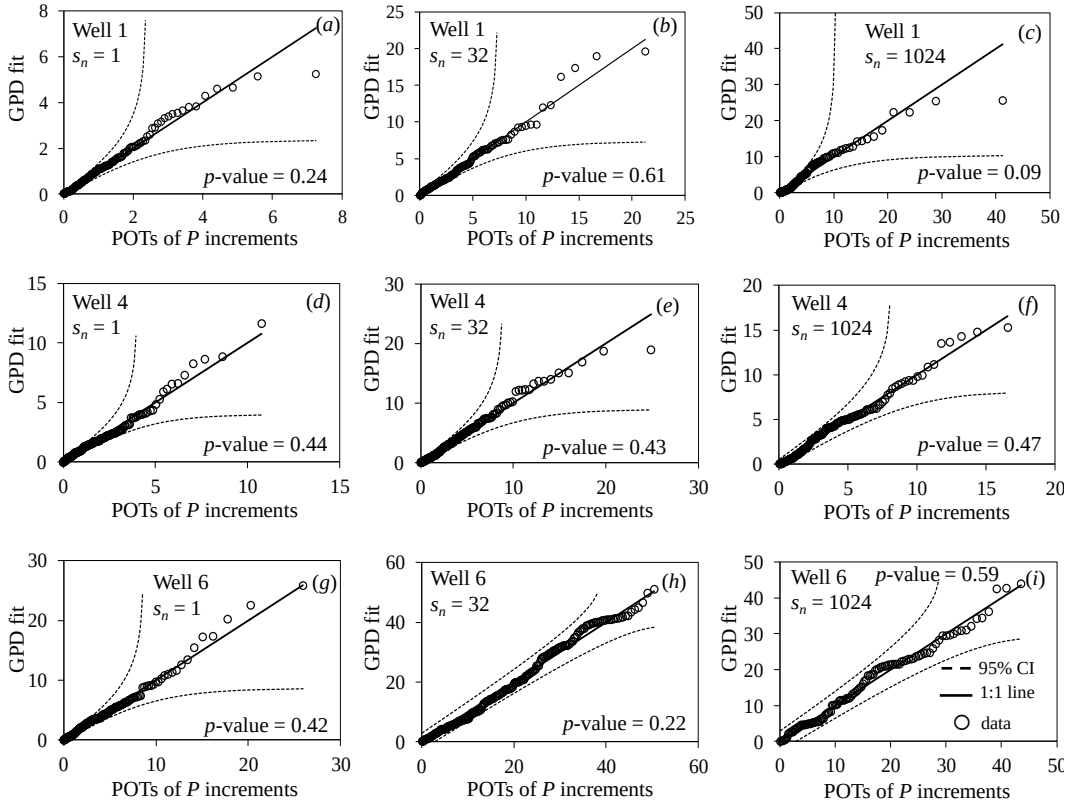

Figure 14. Quantile-quantile plots of GPD fits to frequency distributions of POTs of *porosity* increments at normalized lag s_n = 1, 32 and 1024 in **(a–c)** Well 1 (Maroon), **(d)**–**(d)** Well 4 (Ahwaz), and **(g)**–**(i)** Well 6 (Tabnak). Also shown are a line of unit slope (solid), 95 % confidence intervals (dashed), and *p* values of Kolmogorov–Smirnov tests.

HESSD
11, 11637–11686, 2014

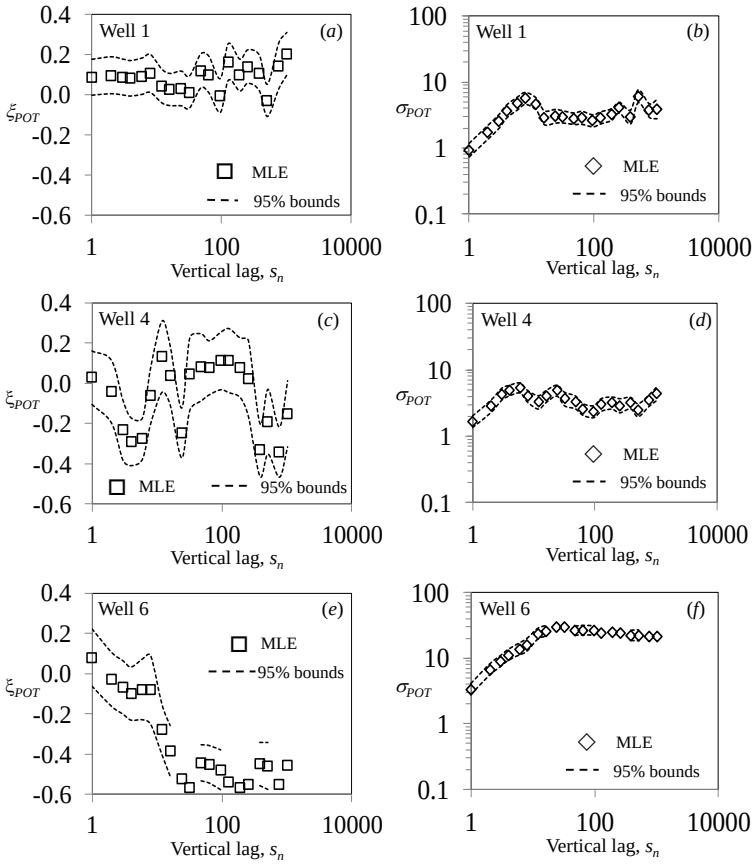

Figure 15. Variations of best fit GPD shape (ξ_{POT}) and scale (σ_{POT}) parameters with normalized lag in **(a, b)** Well 1 (Maroon), **(c, d)** Well 4 (Ahwaz), and **(e, f)** Well 6 (Tabnak). Also shown are 95 % uncertainty bounds.

HESSD
11, 11637–11686, 2014

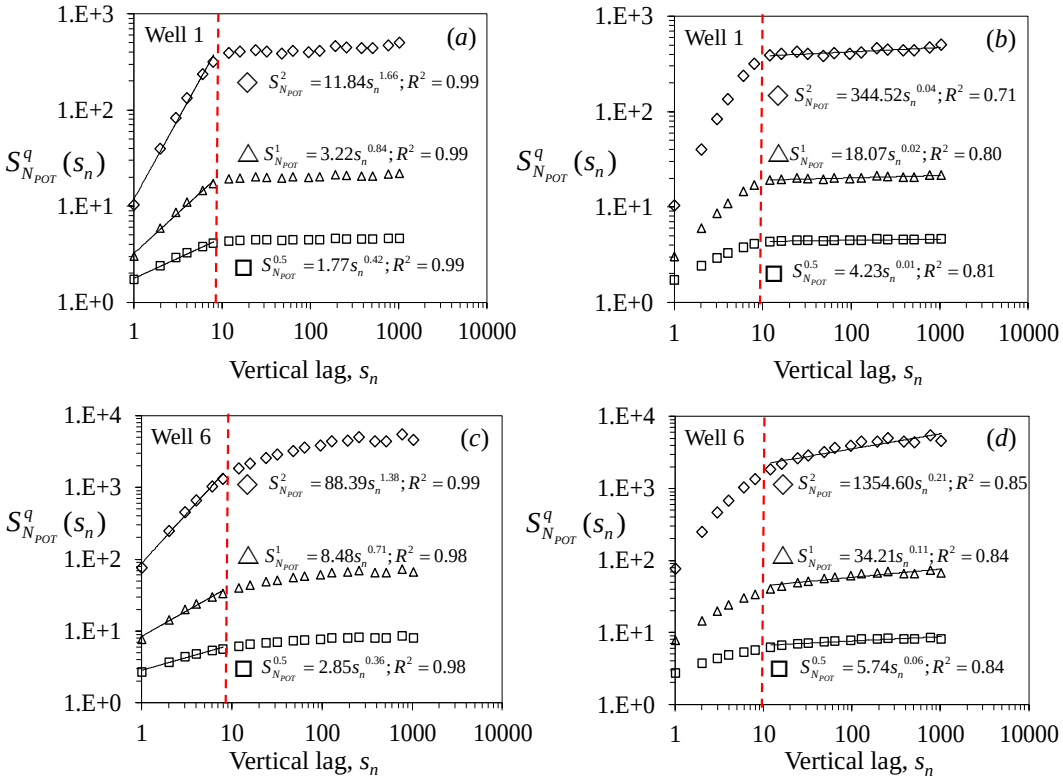

Figure 16. $S^q_{N_{POT}}(s_n)$ vs. normalized lag for q = 0.5, 1.0, and 2.0 in Wells 1 (Maroon) and 6 (Tabnak). Red dashed line demarcates breaks in power-law scaling regimes. Logarithmic scale regression lines and corresponding power-law relations between $S^q_{N_{POT}}(s_n)$ and s_n are given in **(a)** for Well 1 at $s_n < 10$, **(b)** Well 1 at $s_n > 12$, **(c)** Well 6 at $s_n < 10$, and **(d)** Well 6 at $s_n > 12$.

HESSD
11, 11637–11686, 2014

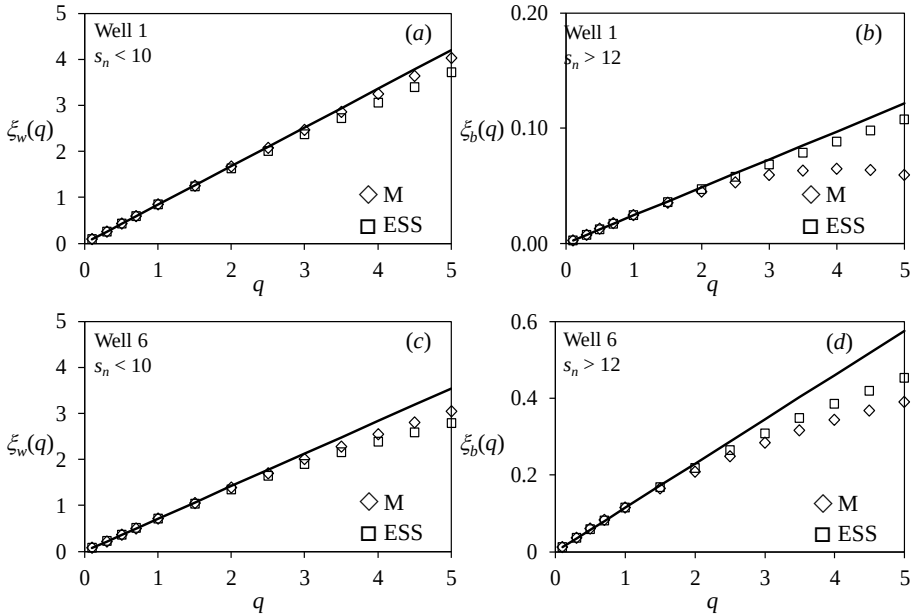

Figure 17. $\xi_w(q)$ and $\xi_b(q)$ evaluated for POTs as functions of q by the method of moments (M) and ESS in **(a)** Well 1 at $s_n < 10$, **(b)** Well 1 at $s_n > 12$, **(c)** Well 6 at $s_n < 10$, and **(d)** Well 6 at $s_n > 12$.

HESSD
11, 11637–11686, 2014